nature neuroscience

Article

https://doi.org/10.1038/s41593-026-02389-8

State-dependent signal flow hierarchy in the human cerebral cortex

Received: 7 October 2024

Accepted: 26 June 2026

Published online: 01 September 2026

Check for updates

Younghyun Oh[1,2,3], Yejin Ann[1,4], Jae-Joong Lee[1], Takuya Ito[5], Sean Froudist-Walsh[6,7,8], Casey Paquola[9], Michael Milham[10,11], R. Nathan Spreng[12], Daniel Margulies[13,14], Boris Bernhardt[12], Choong-Wan Woo[1,2,3,4,15] ✉ & Seok-Jun Hong[1,2,3,4,15] ✉

Understanding how information flows across distributed brain networks is central to linking brain structure, dynamics and function. Here we present a neuroimaging framework that combines integrated effective connectivity (iEC) and unconstrained signal flow mapping for data-driven identification of human cerebral functional hierarchies. Simulations and empirical validation show that iEC recovers connectome directionality and aligns with histologically defined feedforward and feedback pathways. The iEC-derived hierarchy exhibits a monotonically increasing level along the axis where the sensorimotor, association and paralimbic areas are sequentially ordered, consistent with predictions from the structural model of laminar connectivity. This hierarchy is not fixed but flexibly reorganizes across brain states; it becomes flatter during externally oriented processing and steeper during internally focused conditions, reflecting increased engagement of interoceptive regions. Our study indicates that macroscale directed functional connectivity can reveal biologically grounded, state-dependent principles of signal flow in the human brain.

Human cognition arises from the ever-changing dynamical flows of neural information across distributed brain networks. Cortical hierarchy, one of the most fundamental architectures for this dynamic, has been extensively investigated, with early studies[1,2] focusing on the sensorimotor systems and more recent studies[3,4] expanding to the whole-brain level, thereby highlighting its role as a global basis for various cognitive functions. Indeed, evidence from histology[5,6], tract tracing[7] and functional magnetic resonance imaging (fMRI)[8] indicates that the primate brain exhibits a unique organizational axis from the sensorimotor to association cortices, termed 'functional gradient'[3] or 'global processing hierarchy'[3,9]. Although its important role has been repeatedly proven in multiple cognitive domains, such as perception, action and social processing[10–12], as well as typical and atypical brain development[13–15], exactly how a hierarchical organization relates to dynamical neural information flows across the whole brain remains poorly understood.

Two major issues contribute to this lack of understanding: (1) state-dependent functional brain dynamics and (2) the limitations of

[1]Center for Neuroscience Imaging Research, Institute for Basic Science, Suwon, South Korea. [2]Department of Biomedical Engineering, Sungkyunkwan University, Suwon, South Korea. [3]Life-inspired Neural Network for Prediction and Optimization Research Group, Suwon, South Korea. [4]Department of Intelligent Precision Healthcare Convergence, Sungkyunkwan University, Suwon, South Korea. [5]Thomas J. Watson Research Center, IBM Research, Yorktown Heights, NY, USA. [6]Oxford Centre for Integrative Neuroimaging, Nuffield Department of Clinical Neurosciences and Department of Experimental Psychology, University of Oxford, Oxford, UK. [7]School of Computer Science and Statistics and Trinity College Institute of Neuroscience, Trinity College Dublin, Dublin, Ireland. [8]Bristol Computational Neuroscience Unit, School of Engineering Mathematics and Technology, University of Bristol, Bristol, UK. [9]Institute of Neuroscience and Medicine, Forschungszentrum Jülich, Jülich, Germany. [10]Nathan S. Kline Institute for Psychiatric Research, Orangeburg, NY, USA. [11]Center for the Developing Brain, Child Mind Institute, New York, NY, USA. [12]Department of Neurology and Neurosurgery, Montreal Neurological Institute and Hospital, McGill University, Montreal, Quebec, Canada. [13]Centre for Integrative Neuroimaging, FMRIB, Nuffield Department of Clinical Neurosciences, University of Oxford, Oxford, UK. [14]Integrative Neuroscience and Cognition Center, CNRS, Université Paris Cité, Paris, France. [15]Department of Brain Science and Engineering, Sungkyunkwan University, Suwon, South Korea. ✉e-mail: waniwoo@skku.edu; hongseokjun@skku.edu

conventional fMRI connectomics. The former refers to how our brain continuously shifts between different states, often driven by exteroceptive stimuli, such as watching a movie with a high influx of multisensory information, but also by interoceptive signals, such as hunger or thirst reflecting the ongoing physiological states of the body. Even at rest, the brain organizes neural pathways to generate diverse thoughts during mind wandering. Although this 'state-dependent functional dynamic' is a fundamental characteristic of our brain, only a few studies have systematically compared different brain conditions with respect to their dynamics, especially in the context of information flow along the cortical hierarchy.

The second issue is that the current network neuroscience predominantly relies on undirected functional connectivity (FC). Given that the brain functions are ultimately consequences of seamless feedforward (FF) and feedback (FB) interactions, the inability to infer such connectome directionality substantially impedes the field's advancement. This limitation has constantly motivated the field to investigate a 'directed version' of connectome analytics, namely effective connectivity (EC) mapping. This technique, which enables statistical inference of the net influence of one brain area on another, has been increasingly developed in recent studies, now even supporting whole-brain assessment based on fMRI data[16,17]. However, because these methods continue to flourish, EC research is encountering other challenges[18], which are crucial to address to move forward to the next generation of EC approaches. We highlight three such challenges here.

First, many EC methods[17,19–23] have been proposed, each emphasizing its own unique mathematical principle. This diversity, although a testament to the field's vibrant interest, paradoxically led to a lack of consensus among users regarding when and how to employ each algorithm, raising concerns about the reproducibility of their findings[21,24–26]. Second, most EC methods have been validated on the scale of only several dozen brain nodes[21,23,27] (see recent studies[16,17] for exceptions) and rarely focused on dense cyclic and negative connections. Given that the human cerebral cortex has been found to consist of at least 100 functionally distinct areas[28,29], it becomes imperative to develop EC methods capable of analyzing more complex networks to precisely infer functional dynamics in the human brain. Third, biological validation remains scarce. EC algorithms have been typically assessed using artificially built 'synthetic' networks or applied primarily to studies with a fixed hypothesis on the connectivity configuration of a targeted circuit[30,31], thereby limiting the evidence level of human whole-brain studies (but see recent advances[32–34]).

Here we propose a unified imaging framework, termed integrated EC (iEC), to address these challenges. We first undertook an extensive validation of major existing EC algorithms and integrated them into a single iEC framework to synergize the complementary strengths of individual algorithms while obviating the development of another standalone method. Our EC framework has been tested on simulations of biologically plausible networks and compared with empirical tract-tracing and resting-state fMRI data across two network complexities, both comprising more than 100 nodes and dense cyclic connections. It revealed hierarchical connection polarity in the human brain, with unimodal areas predominantly exhibiting positive outgoing connections, whereas heteromodal areas exhibit a balanced ratio of positive and negative connections. Given that these patterns closely mirror known physiological characteristics of FB and FF pathways[35,36], we further leveraged our method to estimate a cortex-wide hierarchical level, which allows us to map signal flows in the human brain. Notably, the identified hierarchy showed a remarkably similar pattern not only to the widely accepted Mesulam's classic model but also to cytoarchitectural cortical types[37], both spanning from low-level sensory (koniocortical) to higher-order (eulaminate and dysgranular) areas, as well as up to the paralimbic (agranular) regions, the latter mainly known for interoceptive monitoring of the internal milieu[38]. Finally, we compared the hierarchy map across the resting, externally oriented (movie watching) and interoceptively focused (tonic pain) states. We found that the cortical hierarchy undergoes considerable state-dependent reorganization, each specific to a given condition. Together, our iEC framework offers a unique opportunity for in vivo mapping of signal flow hierarchy in the human brain and paves the way toward a quantitative delineation of state-dependent network information flow.

Results

Our study consisted of two main phases (Fig. 1). First, we examined individual EC algorithms and categorized them based on their distinct statistical characteristics. We then developed a new approach to integrate their EC results (iEC), which demonstrated substantially improved accuracy through multistep validations. In the second phase, we utilized this iEC to comprehensively examine (1) unconstrained large-scale signal flows; (2) the hierarchy emerging from this dynamic; and (3) its flexible state-dependent reorganization in the human brain.

Specifically, we included the following nine individual EC algorithms, each previously proven to yield high accuracy for directionality mapping: regression dynamic causal modeling (rDCM[17]), vector autoregression (VAR) model[39] (a lag order of 1), multivariate Granger causality (MVGC[40]), fast adjacency skewness (FASK[21]) algorithm, cyclic causal discovery (CCD[41]), best order score search (BOSS[16]) algorithm, direct linear non-Gaussian acyclic model (directLiNGAM[42]), greedy relaxations of the sparsest permutation (GRaSP[43]) algorithm and Patel's τ[44] (Extended Data Table 1). Although non-exhaustive, this set was chosen to cover a wide spectrum of methodological principles, including both graphical and dynamical systems, linear and nonlinear and pairwise and multivariate approaches (Extended Data Fig. 1). We then integrated these algorithms by computing a weighted sum of individual EC estimates, with the weight optimized to maximize correspondence with a target connectivity metric (for example, ground-truth directed networks). To prevent overfitting, the optimization was conducted in a strictly cross-validated manner using Bayesian optimization (see 'iEC framework' in Methods).

Three-step validation of EC algorithms

To comprehensively assess both individual algorithms and iEC, we conducted the following three validation steps: (1) comparison with empirically derived directed anatomical connectivity from the macaque brain via viral tracer injections; (2) simulation utilizing biologically constrained directed networks from diffusion MRI-based structural connectivity (SC); and (3) assessment of the ability of EC algorithms to reproduce dynamics inherent to empirical fMRI signals of the human brain.

Validation using macaque tract-tracing and fMRI data. We began by leveraging macaque tract-tracing data[4] together with resting-state fMRI of 19 anesthetized macaques from PRIME-DE[45], as these resources serve as a gold-standard reference for directed whole-brain connectivity mapping in the primate species (Fig. 2a). First, in the randomly subsampled training data ($n = 8$), we estimated optimal integration weights (β) for each algorithm. The median β values were then used to construct iEC matrices in the test set ($n = 11$). We then compared the resulting EC estimates against the fraction of labeled neurons (FLNs), a tract-tracing measure of directed anatomical connectivity via histological labeling (see Methods for details).

The EC algorithms revealed varying degrees of correlation with the ground truth of FLN data. Notably, their optimized β values indicated that only one or two algorithms per methodological family contributed strongly to the iEC (Fig. 2b): VAR (dynamical systems), LiNGAM and FASK (both graphical models) (one-tailed t-test; $P_{FDR} < 0.001$). Based on this pattern, we constructed two iEC variants: one using all algorithms (full iEC) and another using the top three (VAR, FASK and LiNGAM; top 3 iEC). We then estimated their performance using test macaque subjects (Fig. 2c). Both variants yielded similar accuracies (median $r = 0.60$) and

https://doi.org/10.1038/s41593-026-02389-8

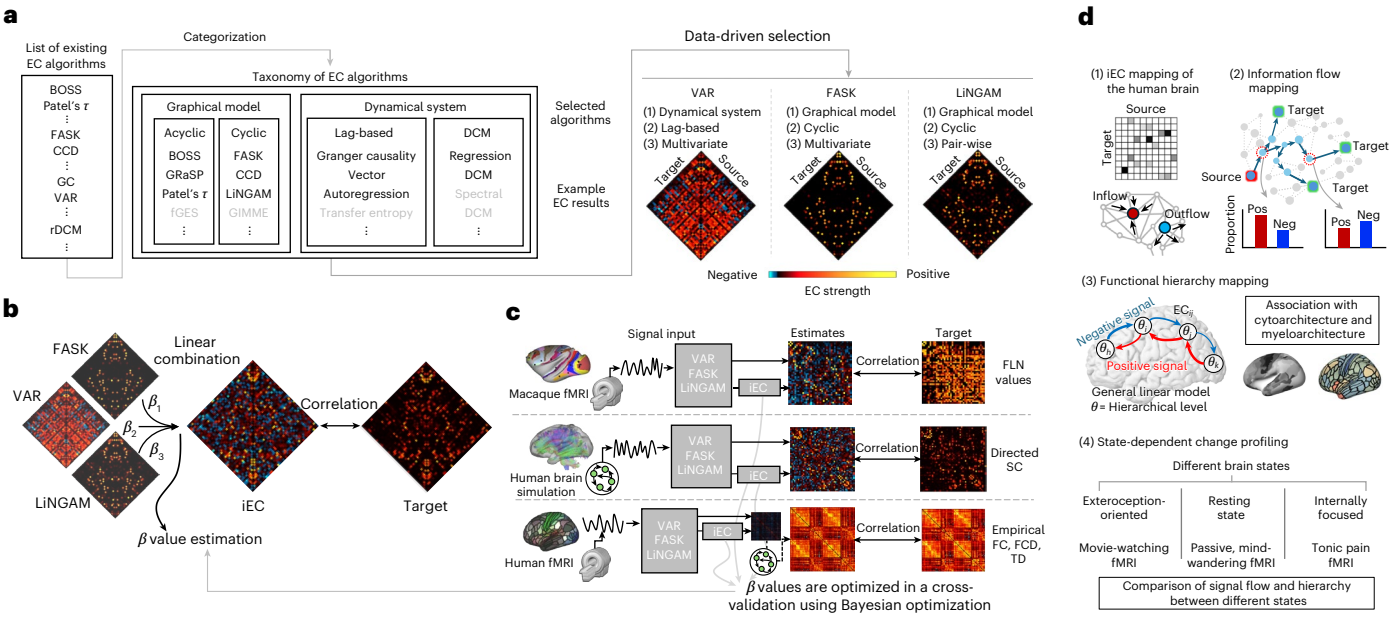

Fig. 1 | Overview of the iEC approach and comprehensive network profiling of the human brain. a, Taxonomy of EC algorithms. After comprehensive research and classification, we have categorized individual EC algorithms into two major groups: one based on 'graphical models' and the other based on 'dynamical systems'. Among these, we selected representative EC algorithms for each category through a fully data-driven validation, which included VAR, FASK and LiNGAM. **b**, Results of individual algorithms were then combined using Bayes-optimized linear integration, which performs a weighted sum of their EC results to create an iEC. **c**, Both individual and iEC algorithms were evaluated through a three-step validation process: (1) empirical fMRI signals from the macaque brain were fed into each EC algorithm, and the results were validated against tract-tracing-based FLN; (2) simulated brain-like signals were input into each algorithm, and the estimated EC was compared to ground-truth synthetic directed SC in the human brain; and (3) empirical fMRI signals from the human brain were input into each algorithm, the resulting EC matrix was used to simulate brain signals and the simulated FC, FCD and TD were compared against empirical data. **d**, After methodological validation, the group-level iEC map from empirical human fMRI was profiled in terms of (1) degree distribution and (2) signal flows across the network. Next, (3) the hierarchical levels across the whole brain were estimated using a general linear model based on the iEC values and evaluated based on architectonic data and finally (4) compared across different brain states, including externally oriented, resting and internally oriented states. Neg, negative; pos, positive.

significantly outperformed the best-performing individual algorithm (median $r = 0.52$; $P_{FDR} < 0.001$; two-sided Wilcoxon signed-rank test). To complement this correlation-based assessment, we also evaluated directionality of identified ECs using an F_1 score across two differently thresholded EC matrices (15% and 30%). Again, iEC outperformed individual algorithms at both thresholds ($P = 0.04$ at 15%; $P < 0.001$ at 30%; Supplementary Fig. 1), confirming the advantage of iEC in the identification of directed connectivities. To understand the source of this advantage, we examined how the three dominant algorithms contributed to constructing iEC (Fig. 2d). This analysis revealed that each algorithm specializes in a different regime of this contribution. Specifically, VAR captured widespread weak-strength connections, whereas LiNGAM and FASK were more sensitive to sparse yet strong connections (Supplementary Fig. 2). Thus, the gain of iEC did not arise from simple averaging but from integrating algorithms that resolve complementary portions of the EC landscape.

Because all algorithms so far have been applied directly to blood oxygenation level-dependent (BOLD) signals, we next asked whether region-specific hemodynamic response (HR) could affect the integrity of our EC estimation. To test this, we repeated the analysis by applying a state-of-the-art brain-area-specific HR deconvolution[46] to empirical BOLD signals (see Methods for details). Most algorithms, with the exception of MVGC, showed high consistency of EC maps between pre-deconvolution and post-deconvolution signals (all other individual methods: $r > 0.8$). This consistency was especially high for the iEC approach ($r = 0.91$; see Extended Data Fig. 2 for the replication in the human brain; $r = 0.87$). Owing to its low consistency for HR effects, MVGC was excluded from all subsequent analyses. Based on these largely intact EC results, together with a previous study showing rather compromised system identification after HR deconvolution[47], in the subsequent analyses we focused on the EC results identified using original BOLD signals.

Inspecting the iEC result from the macaque brain showed that positive ECs are both stronger and more prevalent, whereas negative ECs are generally weak and sparse across the brain areas (Fig. 2a). Previous studies suggested that these connection polarities may reflect intricately mixed excitatory and inhibitory effects, potentially aligned with FF and FB signal pathways[35]. Indeed, although a dominant portion of FF connections has previously been found to target excitatory neurons (thus exerting positive and amplifying influences to target regions)[48], FB connections were associated with both excitatory and inhibitory pathways[49,50], although the latter 'suppressive' effect has traditionally been considered a major characteristic of FB. To assess whether these distinct patterns can also be captured in our macroscale analysis, we profiled the iEC with respect to supragranular labeled neuron (SLN) (fraction of SLNs), a marker to quantitatively index the level of FF and FB connectivity (see 'Macaque tract-tracing data' in Methods). Interestingly, when we categorized iECs into FF or FB by applying a 0.5 threshold to their SLN value (range: 0–1; FF: SLN > 0.5; FB: SLN < 0.5), the majority of iECs categorized to the FF pathway were positive, whereas those assigned to FB showed a more balanced ratio of positive and negative connections (Fig. 2e, right), mirroring previous reports on the physiological nature of FF and FB pathways.

Validation using directed SC networks. Although validation using the macaque FLN confirmed that the iEC framework can reliably capture experimentally defined hierarchical features, its applicability to the human brain remains uncertain because an equivalent directed

https://doi.org/10.1038/s41593-026-02389-8

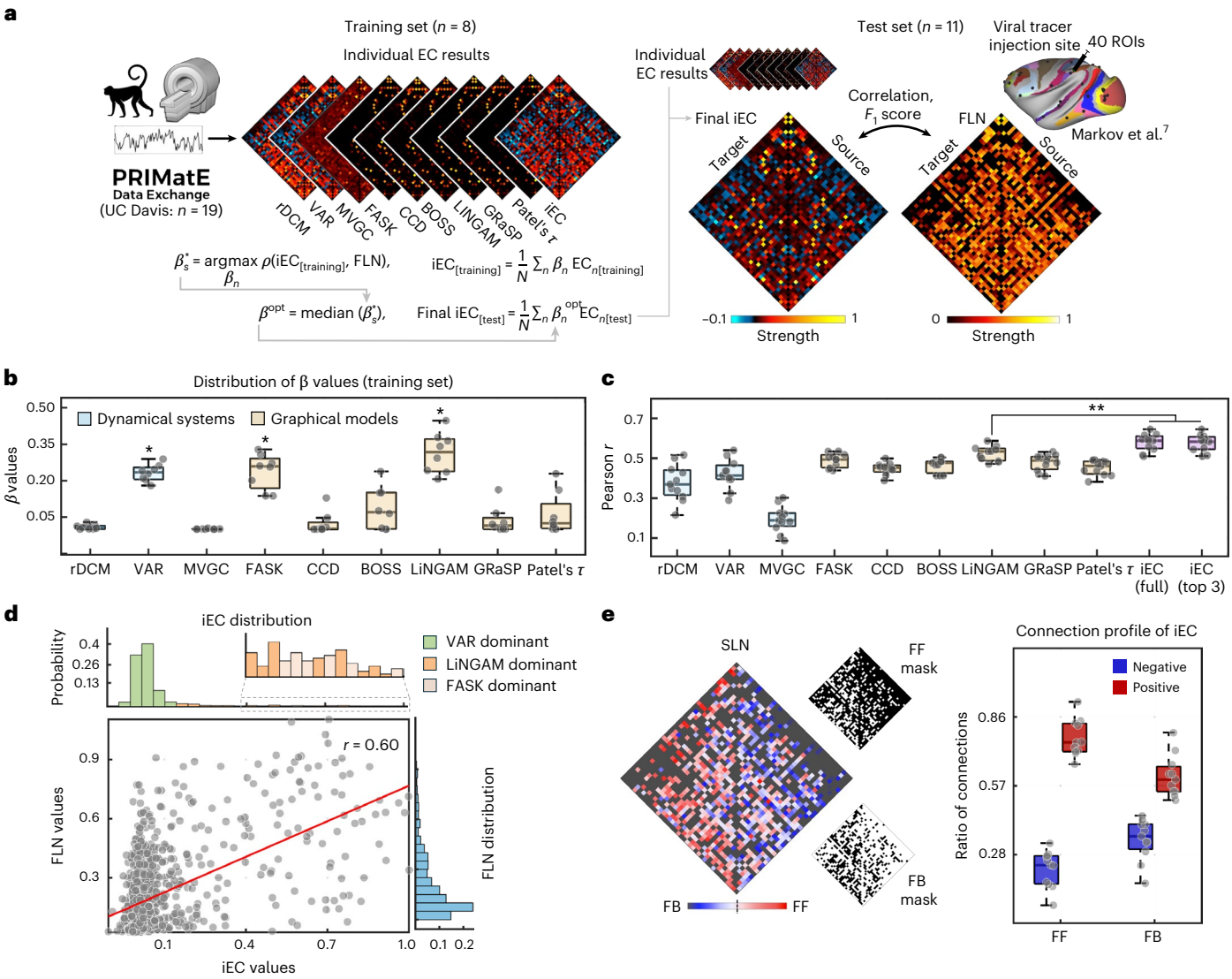

Fig. 2 | Validation of individual and iEC algorithms using macaque tract-tracing data. a, Individual ECs were inferred from anesthetized macaque fMRI data, which were parcellated into 40 regions defined by viral tracer injection sites. Optimal β coefficients for each EC algorithm were derived from the training dataset ($n = 8$ macaques) by maximizing the correlation between iEC and FLN. Using median optimal β values, we constructed iEC from an independent test dataset ($n = 11$) to assess generalizability. **b**, Box plot of optimal β values derived from the training dataset. Each dot represents one macaque ($n = 8$), whereas boxes are color-coded by methodological families: dynamical systems (blue) and graphical models (yellow). Three algorithms (VAR, FASK and LiNGAM) demonstrated notably higher β values ($P_{FDR} < 0.001$ in one-tailed t-test), indicative of significant contribution. **c**, Performance comparison of individual EC and iEC algorithms in the test dataset. Two iEC variants were evaluated: one integrating all nine algorithms and another using only the three algorithms with statistically significant β values. **d**, Profile of algorithm contribution in iEC. Each dot represents a connection weight of a single macaque brain with a median performance for iEC (top 3), showing a correlation of 0.6 with FLN. The FLN distribution exhibited a strong heavy-tail structure (right vertical histogram), with the tail primarily captured by LiNGAM and even more so by FASK (upper landscape histogram). In contrast, VAR primarily captured weaker connections, which, despite their relative weakness, accounted for more than 50% of the total connections. **e**, Connection polarity investigated via SLNs. Connections were categorized into FF and FB pathways based on an unbiased SLN threshold of 0.5, and iEC values were profiled separately for each pathway. For all box plots, the center line indicates the median, the box bounds the 25th/75th percentiles and the whiskers represent the most extreme non-outlier values (hereafter the same for all subsequent figures).

connectivity reference is unavailable. To address this, we devised a carefully curated simulation approach based on the group-averaged SC derived from human diffusion MRI after parcellating the brain with the Schaefer-100[28] and Multimodal Parcellation (MMP)-360[29] atlases. Directionality was introduced by rewiring the edges but only minimally (20% of the connections) to preserve key topologies of the original network (degree distribution, clustering coefficients and global connectedness) (Supplementary Fig. 3). Based on these synthetic networks, we simulated whole-brain neural activity with the Hopf model, an established dynamical framework for oscillatory neural signals[51] (see Extended Data Fig. 3 for replication with a more biophysically detailed model). We then applied the same EC analyses used in the macaque brain, comparing the outputs to the synthetic networks.

Across both low-resolution and high-resolution brain parcellations, the EC results demonstrated high consistency with those of the macaque brain. Indeed, the distributions of optimized β values closely mirrored those from the macaque data (Extended Data Fig. 4a), and the iEC outperformed all individual algorithms in recovering an EC structure across two network resolutions (Extended Data Fig. 4b). Taken together, our simulation provides robust evidence for the resilience and scalability of the iEC framework, supporting its translational value in the human brain.

https://doi.org/10.1038/s41593-026-02389-8

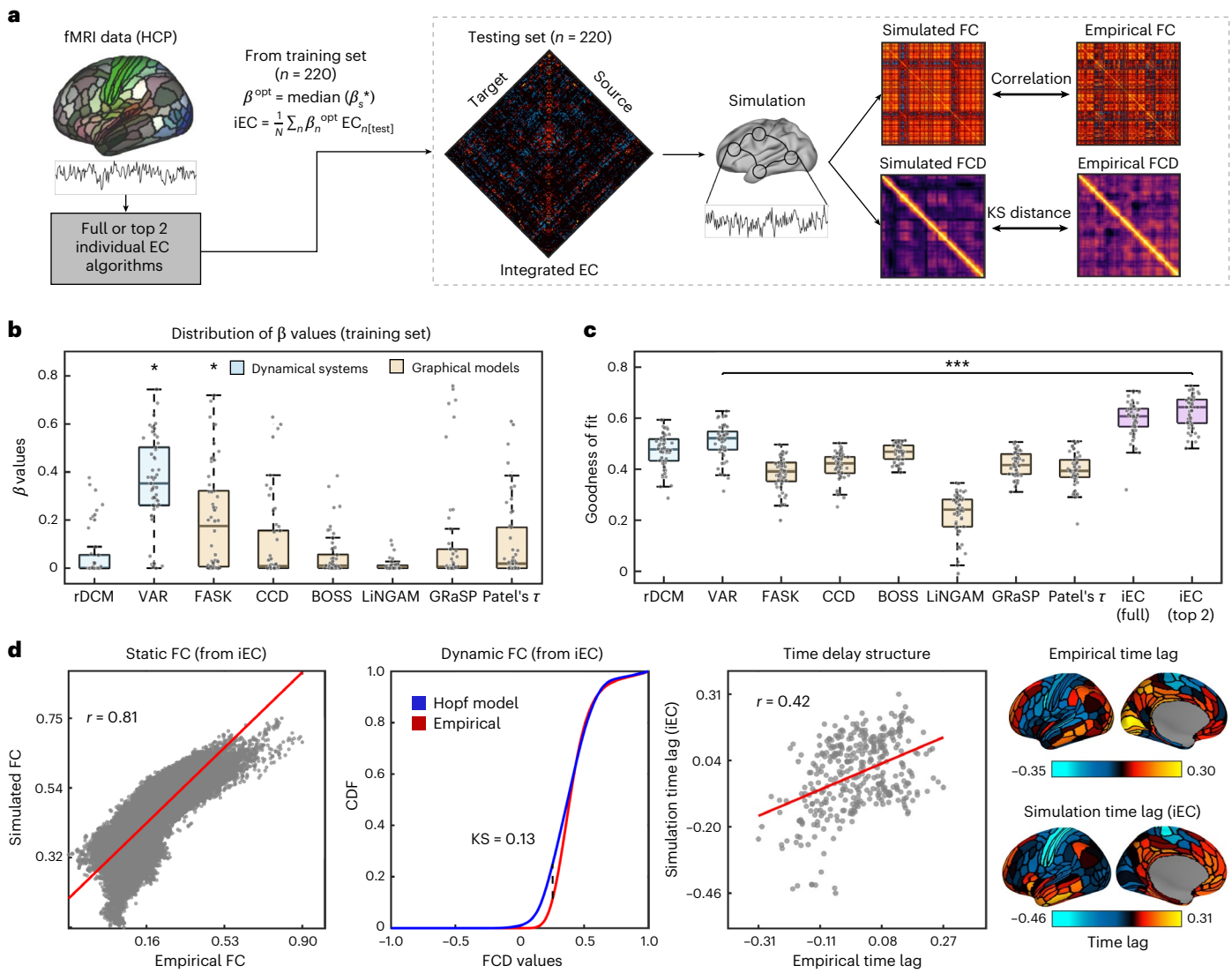

Fig. 3 | Validation of iEC framework using human fMRI data. a, Schematic of the validation. Individual ECs were first estimated from resting-state fMRI data. The iEC was then constructed by integrating individual ECs using the optimal β coefficients from a training set ($n = 220$ participants). For validation, the resulting EC matrices and the constructed iEC were used as a network backbone to simulate fMRI signals via the Hopf model. The simulated time series were then used to compute the FC and FCD, which were compared to their empirical counterparts. **b**, Distribution of the optimized β values across 50 independent runs of Bayesian optimization on the training set. Each dot represents the optimal weight obtained from a single run, reflecting each algorithm's relative contribution to the iEC model. The effect of VAR and FASK was demonstrated to be significant (one-sided t-test against 0; $P_{FDR} < 0.001$). **c**, The overall fit scores of each EC algorithm and iEC were evaluated with a metric of 'static FC correlation minus the FCD KS distance' in a held-out testing set ($n = 220$). Each dot represents one realization of the iterative simulations. Two iEC variants were evaluated: one integrating all nine algorithms and another using only the algorithms with statistically significant β values. Top 2 iEC showed significantly higher fit than the best individual algorithm (two-sided Wilcoxon signed-rank test; $P < 10^{-7}$). **d**, Comparison of empirical and iEC-simulated FC and FCD. Left: each dot represents an FC value between a pair of brain regions. The red line shows the least-squares linear fit. Middle: cumulative distribution functions (CDFs) of FCD from empirical and simulated data. The maximum distance between the Hopf model (blue) and empirical (red) data (vertical dashed line) represents the KS distance between the two distributions. Right: comparison of empirical and simulated TD structures. Each dot in the scatter plot represents the mean time lag of a brain region. Group-averaged delay maps are shown on the cortical surface.

Validation using human fMRI. Finally, we evaluated the EC algorithms using human resting-state fMRI from the Human Connectome Project (HCP) (440 subjects split into training and testing sets). Given the absence of an established ground truth, we adopted a model-based validation strategy to assess how well each inferred EC matrix could reproduce empirical signal properties of the human brain (Fig. 3a). Specifically, we used each EC matrix as a 'directed-connectivity scaffold' for simulating whole-brain dynamics and compared the resulting simulated signals to empirical fMRI data. The rationale for this approach was that, should the inferred EC effectively approximate an inherent structure of whole-brain information flows, the resulting simulated dynamics would closely replicate its empirical counterpart.

To test this, we employed two complementary metrics: static FC and functional connectivity dynamics (FCD). To quantify their combined effect, we adopted a composite score from previous studies[52,53], defined as Pearson correlation (r) between empirical and simulated FC minus Kolmogorov–Smirnov (KS) distance between their FCD distributions (fit = r − KS). A higher score signifies a closer match between the signal properties of the simulated and empirical data. We leveraged this score to optimize β for each algorithm in the construction of iEC within the training data. Our analysis focused on group-level results from the MMP-360 atlas (see Extended Data Fig. 5 for the results of Schaefer-100). Upon examining the optimized β values, we found that only VAR and FASK made significant contributions to iEC estimation

https://doi.org/10.1038/s41593-026-02389-8

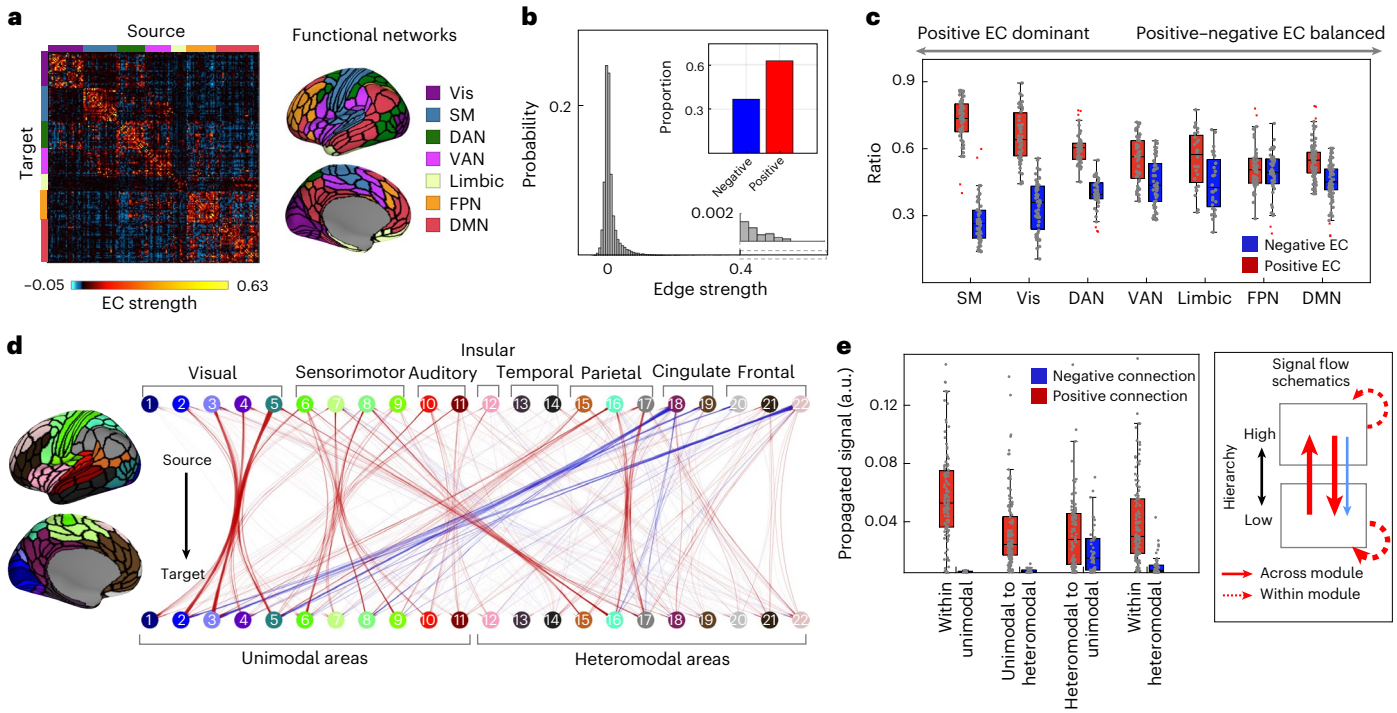

Fig. 4 | The iEC profiling of the resting-state human brain. a, The modular structure of iEC is unveiled by organizing it according to the seven different functional networks of the Yeo–Krienen atlas. **b**, The edge distribution of iEC shows a characteristic heavy-tail distribution. **c**, Profiling of the positive–negative ratio of out-degree connections based on the seven functional networks (each dot represents a cortical region from the group-level iEC; see Extended Data Fig. 6c for in-degree). Note that the dichotomized pattern between positive and negative connections in the unimodal regions gradually converges into a form with a more balanced ratio in higher-order heteromodal areas. **d**, Signal propagation based on a linear dynamical system[57] across 22 modules of the MMP-360 atlas. Modules are categorized into functionally specialized subnetworks for easier interpretation of the signal flow patterns. Edge thickness indicates signal strength, and color represents positive (red) and negative (blue) signal flows, respectively. **e**, Stratification of signal propagation based on the proportion of positive and negative signal flows within and between unimodal and heteromodal systems. Each dot represents one intermodule signal flow. SM, somatomotor; Vis, visual; DAN, dorsal attention network; VAN, ventral attention network; FPN, frontoparietal network; DMN, default mode network.

(one-tailed t-test; $P_{FDR} < 0.001$; Fig. 3b). This finding closely aligns with the algorithmic contributions in the macaque brain, underscoring the robustness of our iEC method.

Based on this observation, we constructed two variants of iEC: one incorporating all algorithms (full iEC) and the other limited to those with significant contributions (top 2 iEC) and assessed generalizability on the held-out testing set. The EC results from these two models were consistent with the findings in the macaque brain (Fig. 3c). Specifically, both iEC variants significantly outperformed the best-performing individual algorithm (VAR). In fact, the top 2 iEC yielded an even higher fit compared to the full iEC (Wilcoxon signed-rank test; two-tailed; $P = 0.013$), highlighting an advantage of implementing a parsimonious EC model. When evaluating the two metrics comprising the fit score (Fig. 3d), the simulated FC was highly correlated with the empirical FC ($r = 0.81$), and their FCD distributions were also closely matched (KS = 0.13; the value closer to zero indicating a better model fit), suggesting strong fidelity in both spatial and temporal domains. We also investigated another dynamics-sensitive measure called time delay (TD), which quantifies an intrinsic lag relationship across the brain regions[54]. Although TD was not included in the β optimization process, iEC-based simulations reproduced empirical TD with high similarity ($r = 0.42$). Collectively, these multilevel assessments support the validity of iEC across network complexities and species, as well as its ability to capture network dynamics.

Investigation of iEC profiles and signal flow hierarchy in the human brain

Profiling of the human whole-brain iEC. Having validated our iEC method, we next applied it to the resting-state fMRI of 220 healthy subjects (test dataset) to characterize human whole-brain group-level EC architectures. The connectivity matrix sorted out by the Yeo–Krienen functional networks revealed distinct modular structures (Fig. 4a); within-module connections were predominantly positive, whereas the between-module ones were largely negative, which may reflect a nature of functional organization in terms of network integration and segregation. Furthermore, in line with previous electrophysiological and tract-tracing evidence[55], the human brain ECs also exhibited a heavy-tailed connectivity distribution (tail index = 1.45; Fig. 4b), indicating the presence of infrequent yet strong positive connections. In contrast, the negative connections showed the complementary pattern, characterized by weaker but considerably prevailing ECs across the entire brain (40%).

Next, we examined the directionality of iEC with respect to two network indices: weighted degree distribution and intrinsic signal flow. First, when we separately estimated positive and negative out-degree iECs (see Fig. 4c for out-degree ECs and Extended Data Fig. 6 for in-degree ECs), the sensory cortices showed a clear dominance of positive connections, whereas in more hierarchically higher areas (for example, heteromodal or limbic), they exhibited a more prominent ratio of negative connections. Indeed, when we categorized them based on a previously established network-level hierarchy[56], this gradient of signed connection polarity was clearly observed, and it is well aligned with the previous macaque result (Fig. 2e; mostly positive ECs from FF versus a balanced presence of positive and negative ECs from FB).

To move beyond degree measures and ask how this connectivity structure shapes inter-area signal transmission, we employed a recently developed linear dynamical system approach[57] to model unconstrained

https://doi.org/10.1038/s41593-026-02389-8

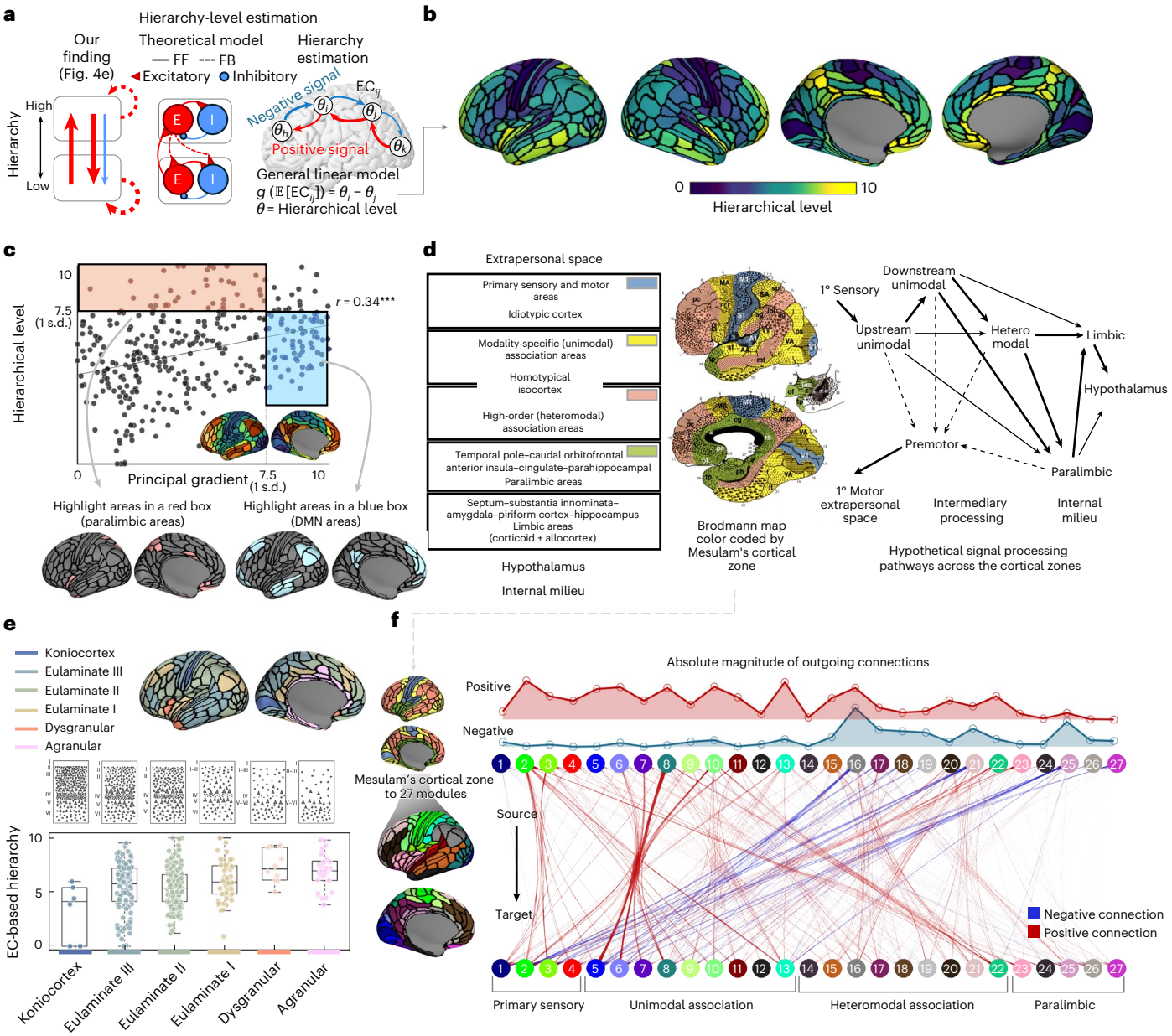

Fig. 5 | The iEC-derived signal flow hierarchy in the human brain. a, Schematic of our approach to estimate the hierarchy. To illustrate the process of hierarchy determination, we put side by side a previous diagram of hierarchical signal flow (Fig. 4e) and its theoretical laminar model. Inspired by FLN-based hierarchy determination in the macaque brain, we used the iEC matrix to infer the hierarchy level across the entire human brain. **b**, The resultant iEC-derived hierarchy map is shown. The insular and paralimbic areas are positioned at the top of the hierarchy, whereas the sensorimotor areas are located at the bottom. **c**, Difference between our EC-based hierarchy and the FC-based functional gradient. Brain areas with higher EC-based hierarchy (>mean + 1 s.d.) but lower functional gradient (<mean − 1 s.d.) are marked in red, whereas those with opposite profiles (higher gradient but lower hierarchy) are marked in blue in both graphs and cortical surfaces. **d**, Cortical zones proposed by Mesulam[9] (left), indicating different levels of cortical hierarchy. Note that within the neocortex, the paralimbic areas are at the top of the hierarchy. These four zones are superimposed on the Brodmann parcellation (middle). The hypothetical signal-processing pathways across hierarchical levels proposed by Mesulam are shown (right). All figures are sourced from a previous study[9]. **e**, Relationship between the EC-based hierarchy and histological cortical types (each dot represents a cortical region). **f**, Signal flow was analyzed across 27 modules derived from Mesulam's cortical zones. Positive signals originating from primary and unimodal areas decreased along the hierarchy, whereas negative signals progressively occupied the emission of higher-order areas. Panel **d** reproduced with permission from ref. 9, Oxford Univ. Press. Cortical-type schematic in **e** adapted from ref. 37, under a Creative Commons license CC BY 4.0.

signal propagation from predefined seed areas (Fig. 4d and Methods). This analysis revealed that positive signals predominantly originate from hierarchically lower cortical areas, whereas negative signals are almost exclusively sent from the higher-order to lower-order regions. Moreover, both unimodal and heteromodal areas showed strong positive signaling within their own modules, suggesting the presence of specialized local subsystems embedded within the broader hierarchy (Fig. 4e). In sum, our findings show that iEC has high potential to recapitulate the principle of signal flows across the areas with varying hierarchical levels.

Retrieving signal flow hierarchy from iEC. The iEC analyses so far have provided converging evidence that it could capture a silhouette of hierarchical brain organization, including (1) a robust relationship

https://doi.org/10.1038/s41593-026-02389-8

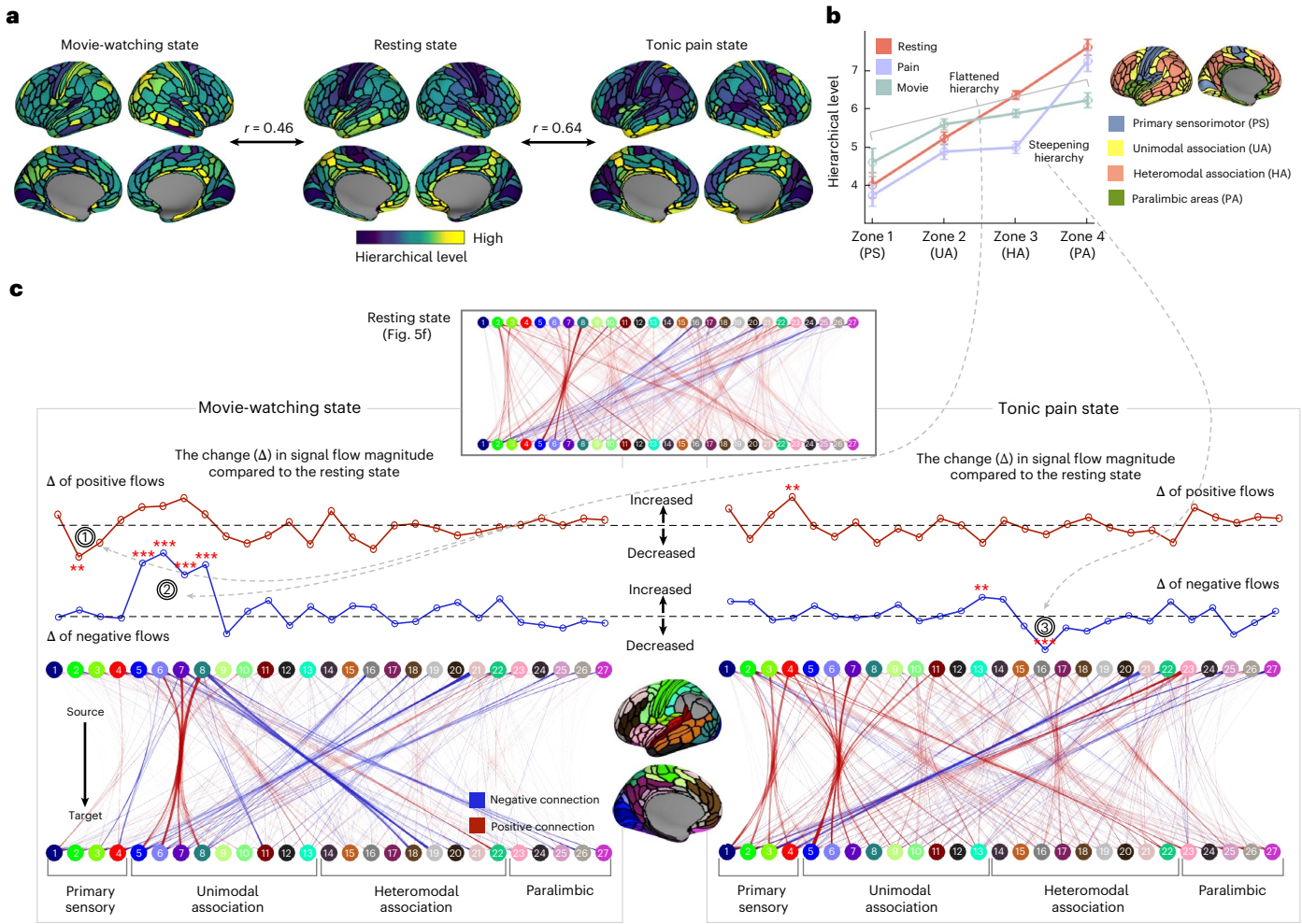

Fig. 6 | State-dependent reorganization of cortical hierarchy and signal flow of the human brain. a, Signal flow hierarchy maps derived from movie watching (left), resting (middle) and tonic pain (right) states. The correlations of their spatial patterns are shown between the states. **b**, State-dependent changes in hierarchy levels sorted out based on Mesulam's four cortical zones (primary sensorimotor, unimodal association, heteromodal association and paralimbic areas). Note that the movie-watching state resulted in a flattened cortical hierarchy, whereas the tonic pain condition accentuated the disparity between paralimbic and non-paralimbic areas (steepened hierarchy). **c**, Signal flow analysis across 27 modules of MMP (parcellated according to the cortical zones) in the movie-watching and tonic pain states. Top: the magnitude of changes in signal flows (Δ) in these states compared to the resting state is presented as a line graph, separately for positive and negative streams. Module-wise Δ values were *z*-scored across the 27 modules and converted to two-sided *P* values; false discovery rate (FDR) correction was applied separately to positive and negative streams. **Uncorrected $P < 0.05$; ***$P_{FDR} < 0.05$. Bottom: in the graph, the findings of 'decreased positive signal flow' and 'increased negative signal flow' are both related to enhanced hierarchy at the primary sensory and visual association areas. Similarly, ③ 'decreased negative signal flow' in the default mode area means its diminished hierarchy during a tonic-pain condition, which may cause the steepened hierarchy in this brain state.

between iEC patterns and FF/FB connectivity in the macaque brain (Fig. 2e); (2) a different proportion of positive/negative signaling along the sensory–association axis in the human brain (Fig. 4c,d); and (3) the observation that the majority of negative signal flows occurred in the heteromodal-to-unimodal pathways (Fig. 4e). These observations collectively motivated a direct test of whether iEC could be used to estimate cortical hierarchical level.

To answer this question, we adopted an established modeling framework[7], originally designed in macaque studies to quantify cortical hierarchy from FF and FB connectivity. Although this framework traditionally relies on histological data (for example, SLN values), our preceding results suggest that the signed iEC matrix contains analogous information from which we could infer directional signal asymmetry (Fig. 5a). We therefore used the group-level iEC matrix as a substitute for SLN to reconstruct a signal flow hierarchy of the human brain using this framework (see Supplementary Fig. 4 for replication using held-out dataset).

Mapping this hierarchy revealed a distinct and organized structure (Fig. 5b): primary sensory and motor areas occupy the lowest tiers, whereas paralimbic cortices, such as the anterior cingulate, insular and parahippocampal regions, are positioned at the highest levels of cortical hierarchy. This pattern was partly comparable, yet remained distinct from a well-established functional gradient[8], a dimension-reduced topographic map of undirected FC running on a sensory–association axis (Fig. 5c). Although the EC-based hierarchy was significantly correlated with the functional gradient ($r = 0.34$; $P < 0.001$), paralimbic regions exhibited higher values exclusively in the EC-derived hierarchy map. This emphasis on the paralimbic regions aligns with Mesulam's initial proposition[58], in which these regions were conceptualized as a 'neural bridge' linking the neocortex and interoceptive areas monitoring the internal milieu (Fig. 5d). The validity of our EC-based hierarchy map was further supported by post hoc cytoarchitecture and myeloarchitecture analyses (Extended Data Fig. 7a). When cortical regions in Campbell's atlas[59] were sorted based on their hierarchical values, the

pattern closely matched a known hierarchy stream: from primary sensory areas to unimodal and heteromodal association areas and finally to paralimbic areas. A significant correlation with myeloarchitecture (by Nieuwenhuys's atlas depicting a cortical myelin level[6]) was also found ($r = 0.42$; $P < 0.001$), underscoring the relationship between the signal flow hierarchy and its anatomical substrates[60].

Most importantly, our validation drew upon the seminal structural model theory[61], which posits that FF and FB connections depend on the laminar structure of the connected areas. According to this model, FB connections typically originate from areas with simpler laminar structures ('agranular' or 'dysgranular') and target areas with more elaborate laminar structures ('eulaminate' or 'koniocortex'), and vice versa for the FF connections. Inspired by this theory, we tested our hierarchy map by examining its whole-brain profile across different cortical types (Fig. 5e). This analysis revealed a highly significant alignment (general linear model; $t = 5.14$; $P < 0.001$), with a progressive hierarchical increase matching decreased granular layers (see Extended Data Fig. 7b for the result with the functional gradient). Finally, we reexamined unconstrained signal flow after sorting cortical areas according to Mesulam's cortical zones. This analysis revealed that the progression of signed signaling closely matched FF and FB motifs implied by the hierarchy map (Fig. 5f): primary sensory and unimodal association areas predominantly emitted positive signals, heteromodal regions exhibited a more balanced mixture of positive and negative signal flow and paralimbic regions were characterized almost exclusively by negative signal emission.

State-dependent reorganization of signal flow hierarchy. Although the hierarchy derived from a resting state showed compelling biological evidence, it represents only a single brain state, characterized by the absence of explicit environmental engagement. We therefore asked whether this hierarchical structure stays stable across brain states, or whether it is dynamically reconfigured to adapt to changing contextual demands.

To test this, we analyzed two additional fMRI datasets representing major non-resting brain states. The first was acquired while watching a movie (*Forrest Gump*), capturing an externally focused (exteroceptive) state, and the second was scanned during the experience of tonic pain induced by oral capsaicin eliciting an internally focused (interoceptive) state. For each state, we reconstructed the hierarchy using the same procedure applied to the resting state. When directly correlating the spatial pattern of whole-brain hierarchy, its global trend was largely preserved in both movie-watching and tonic pain states compared to the rest (Fig. 6a; $r = 0.46$ and 0.64, respectively; both $P < 10^{-19}$). Yet, scrutinizing the details of each state displayed its idiosyncratic hierarchical changes (Fig. 6b). As previously shown, the resting state showed a monotonically increasing hierarchy across the cortical zones. During the movie-watching state, however, the primary sensory and unimodal association areas showed an elevated hierarchy, whereas the heteromodal association and paralimbic areas exhibited an opposite pattern, overall suggesting a signature of 'flattened cortical hierarchy', consistent with recent findings from naturalistic fMRI[62]. Signal flow analysis provided a parsimonious account of this change (Fig. 6c, left), in which we observed (1) an overall decrease in positive signals from the primary sensory areas and (2) reduced negative signals from paralimbic areas, collectively resulting in less differentiated hierarchical levels across the whole brain. This state-dependent reorganization during movie watching suggests a shift in cognitive load toward externally oriented processes, as indicative of altered FF and FB signaling along the sensory and attention pathways[63,64].

In contrast, in the sustained pain condition, we observed an opposite pattern: a 'steeper' hierarchy formed between the paralimbic and non-paralimbic areas (Fig. 6b, pale purple). Again, signal flow mapping provided a parsimonious account for this change, demonstrating a decreased negative signal emission from the heteromodal association areas (particularly from the angular gyrus; Fig. 6c, right), which may cause their hierarchy levels to diminish (thus resulting in a larger disparity between the heteromodal and paralimbic areas). Unlike the movie-watching state, this reorganization concentrated negative signaling more strongly from the paralimbic system, which may reflect the prioritization of an allostatic control to cope with sustained pain[65]. Finally, despite these state-dependent shifts, a common motif persisted across all three conditions: strong negative signal emission from 'paralimbic/heteromodal to unimodal' regions (especially from the cingulate and orbitofrontal areas; Fig. 6a). Thus, although the broad spatial backbone of functional hierarchy is partly preserved across states, the degree of hierarchy and its detailed functional dynamics are flexibly reweighted according to external and internal dynamics.

Discussion

Ever since Hubel and Wiesel's discovery in the visual cortex[66], functional hierarchy has been a central topic in systems neuroscience, serving as a primary basis for studying the principle of neural information flow. Although early studies focused on sensory hierarchy[67], over the last two decades this notion has expanded to emphasize its whole-brain representation spanning from sensorimotor to association areas[3,4,48,57,60]. In this study, we reconstructed a signal flow hierarchy of the human cerebral cortex in a fully data-driven manner by analyzing different brain states across multiple fMRI datasets. Given that the hierarchy is inherently organized by 'directed' FF and FB pathways[7,68], we employed macroscale EC, linearly combining the results of existing individual algorithms (iEC). This collective inference not only boosted the accuracy of directionality estimation but also revealed interesting relationships between signed (positive and negative) connections and histologically derived FF and FB pathways, providing a crucial hint to infer a hierarchical structure from in vivo fMRI. Our signal flow hierarchy showed strong alignment with the spatial distribution of hierarchy-indexed cytoarchitectonic and myeloarchitectonic features and the laminar proportion of granular cells, effectively recovering the 'sensorimotor–association–paralimbic' axis originally proposed in Mesulam's cortical zone. Moreover, this functional axis does not always adhere to the same hierarchy observed at rest but reorganizes dynamically according to brain conditions, potentially enhancing behavioral adaptability to rapidly changing environments. Our findings offer a new avenue to quantitatively probe state-dependent neural information flows along the biologically validated signal flow hierarchy in both typical and atypical human brain conditions.

The idea that fMRI-based iEC enables the estimation of cortical hierarchy was built upon multiple observations on our iEC profiles and their interpretation in light of previous literature. Traditionally, the FB connections (for instance, those between the cortex and thalamus) were primarily considered to exert a modulatory (often inhibitory) effect, refining bottom-up sensory information[69,70]. However, emerging evidence indicates a more active role of FB connections, not only as a modulator but also as a driver increasing neural activity (excitatory)[71,72], especially for hierarchically proximate cortical areas[49,50]. In contrast to such mixed neurophysiological effects of FB, FF connections have been almost exclusively associated with excitatory effects on the targeted area (but see recent perspectives[73]). For example, experimentally silencing macaque V1 through cooling strongly suppresses neural activity across hierarchically connected areas from V2 to V5/middle temporal, highlighting the driving role of FF pathways[74,75].

Importantly, these distinct excitatory–inhibitory patterns between FF and FB connections also seem observable in our macroscale iEC profiles, assuming that positive iEC generally represents an excitatory effect, whereas negative iEC relates more to an inhibitory effect. Parallel to this notion, when associating the sign of iEC and SLNs, a histological metric quantifying the degree of FF and FB pathways in the macaque brain, we found a unique 'signed iEC asymmetry' gradient: FF connections, as determined by SLN, showed a disproportionate

ratio of positive iECs, whereas FB connections additionally exhibited a marked increase in negative iECs, resulting in a more balanced distribution. A similar asymmetry gradient was observed in the human brain, in which low-level sensory areas, key sources of FF signaling[74,76], showed a dominant proportion of positive iECs, whereas the higher-order association areas (major sources of FB signaling[77,78]) displayed progressively enhanced negative iECs. This cross-species convergence, together with the hypothesized role of FF and FB connections, suggests that despite its macroscale nature derived from fMRI, iEC may contain biologically meaningful signals to infer the trace of FF and FB connections, providing a testable ground to reconstruct the functional hierarchy in vivo.

Our iEC-based method revealed several biologically noteworthy findings in hierarchy mapping. First, compared to the widely used connectome compression approach (functional gradient[8]), which places the default mode network at the apex of the hierarchy, our iEC-based hierarchy map emphasizes the paralimbic regions to characterize a hierarchical stream of the human brain, paralleling Mesulam's original proposition[9]. This suggests that although many studies currently frame the sensory-to-association axis as a major functional organization principle, the axis should also incorporate the interoception-related cortical areas as yet another pivotal anchor. This finding highlights the importance of homeostatic and allostatic regulation of the internal environment in goal-driven interactions with the external world and is supported by our observation on the elevated paralimbic hierarchy (with flattened hierarchy elsewhere) during the tonic pain condition (Fig. 6b), suggesting that the brain may inherently prioritize interoceptive over exteroceptive inputs in certain contexts. Second, the validity of our hierarchy was corroborated by histological architectural maps[6,59] and cortical type analysis based on the 'structural model of laminar connectivity'[5,61]. Notably, when we compared this hierarchy to the one reconstructed based only on the positive iEC (thus attributing their difference to negative iECs), the paralimbic areas with a diminished laminar organization (dysgranular and agranular cortices) exhibited the largest hierarchy changes across the entire brain (Extended Data Fig. 8), suggesting a substantial contribution of negative iECs in capturing the properties of hierarchically higher-order cortical regions, particularly their potential FB modulation effects.

Our findings underscore the importance of dynamic and flexible reconfiguration of the signal flow hierarchy according to brain states. This phenomenon, termed 'state-dependent hierarchical reorganization', is critical for adaptive brain function. Despite the largely static nature of its 'anatomical' hierarchy, the state-dependent mechanism enables transient reconfiguration of the large-scale functional architecture, allowing the brain to effectively respond to moment-by-moment environmental and task-related changes, thereby enhancing its overall viability. Notably, a seminal study[1] had already conjectured this possibility: 'Another possibility is that a hierarchy exists only in a loose sense, for instance, at the level of the different cerebral lobes, but not in any precisely definable manner for individual cortical areas'. Drawing an analogy with human societies, '…Some organizations have an utterly rigid hierarchy, in which every individual knows precisely his or her place within a pecking order. Others are less well defined… may be inherently fluid and context dependent, in that one person ranks above another in one particular circumstance but below the other in another circumstance'. Our discovery of state-dependent reorganization offers new insights into how the brain forms such a context-dependent cortical hierarchy, with the flexibly elevated or flattened hierarchy in specific cortical regions across different environmental contexts exemplifying this phenomenon. This will provide a critical hint for understanding functional brain adaptability, especially when implementing biologically more detailed circuit mechanisms such as neuromodulatory controls via cortico-subcortical loops[79].

Beyond the biological implications, our findings also offer methodological insights for large-scale network simulations of the human brain, a field recently garnering great attention in computational and clinical neuroscience[80,81]. Although a previous study focused on biophysical parameters governing 'local' dynamics (for example, recurrent excitatory and inhibitory-to-excitatory connections)[82], recent evidence increasingly indicates that area-specific properties of long-range connections are also critical in shaping macroscale dynamics[83,84]. In parallel, our findings highlight the role of heterogeneous connectional topology and properties, such as the embedding of cortical hierarchy, directed signal flows and their weighted signs, in simulating more brain-like functional dynamics. Indeed, our post hoc analysis showed that 'negative' iECs, despite their substantially weak strength, are essential for capturing cortical hierarchy in paralimbic regions (Extended Data Fig. 8). Amid ongoing debates regarding the role of macroscale inter-areal connections in shaping spatiotemporal brain activity patterns[85,86], our study underscores the necessity of accounting for heterogeneity in global connectivity structures, an aspect largely overlooked in previous modeling research.

Pioneered by Friston et al. in 2003, EC has evolved to encompass concepts such as directed FC and information flow[87]. Although decades of methodological advances have produced a proliferation of algorithms for estimating directionality, overabundant methods—each tailored to specific modeling assumptions or limitations—have made it difficult for researchers to select the most appropriate approach for their scientific questions. Developing a unified framework rather than yet another isolated algorithm is thus a critical step forward, supported by a comparative study showing that simultaneously leveraging diverse statistical measures provides a more robust approach to dependence estimation than any single metric[88]. Our framework rests on two key properties: (1) EC algorithms empirically and theoretically cluster into distinct methodological categories and (2) algorithms within the same category exhibit high redundancy, whereas those across categories offer complementary information. For example, dynamical-systems-based algorithms produce dense Gaussian-like edge distributions, whereas graphical-model-based algorithms yield sparser ones with heavy-tailed distributions. Even within graphical models, the multivariate (for example, FASK) versus pairwise (for example, LiNGAM) distinction—reflecting whether indirect, multi-hop pathways are considered—further modulates EC-matrix sparsity. Crucially, our data-driven integration exploits these topological characteristics in a context-dependent manner: it does not simply rank these algorithms but adapts to the objective. For example, to reconstruct dense anatomical architectures (such as FLN), the framework prioritizes the high-sensitivity pairwise algorithm (LiNGAM), maximizing edge recovery. Conversely, to simulate complex brain dynamics—in which false-positive connections are likely detrimental to model fidelity—the framework shifts toward the high-specificity multivariate algorithm (FASK), which rigorously prunes redundant pathways. Thus, the integration weights function as a sophisticated mechanism, selecting a minimal and complementary set of algorithms optimized for the specific biological context. This approach shows superior accuracy across parcellation schemes and species (human and macaque) and recovers both static and dynamic features of empirical brain data in whole-brain simulations. Together, our framework offers a streamlined, cohesive pathway for EC mapping in the human brain.

Several limitations should be acknowledged. First, region-specific variability in hemodynamic response function (HRF) can theoretically confound directed connectivity estimates. Although spatial and temporal averaging of macroscale fMRI may linearize signal dynamics and partially mitigate this effect, neurovascular coupling remains a concern; higher-resolution imaging or multimodal data (for example, concurrent electroencephalography–fMRI) will be essential to separate intrinsic neural interactions from vascular confounds. Second, unlike resting or tonic-pain conditions, movie watching involves correlated audiovisual inputs that can induce spurious coactivations[89]. Although this shared variance could distort connectivity estimates, it may also reflect genuine multimodal integration driving signal-flow-hierarchy

reorganization toward external demands; explicit stimulus-feature models (for example, movie-encoding analyses) will help disentangle input-driven synchrony from exteroception-induced signal propagation. Third, our linear weighting strategy, although preserving topological properties, computational efficiency and interpretability, may miss some nonlinear interactions among algorithms. Finally, we excluded subcortical structures (for example, thalamus and hippocampus) because Barbas's structural model—the theoretical basis for hierarchy construction—is cortex-centric, relying on laminar-specific FF and FB projections. Moreover, owing to the characteristic low signal-to-noise ratio of fMRI signals in deep brain structures, iEC profiles computed over the entire brain showed almost negligible EC magnitudes in those areas, yielding a cortical hierarchy map virtually identical to the one including subcortical structures (correlation between maps with and without subcortices; $r = 0.96$). Future studies using higher-gradient field MRI data may scrutinize the effects of subcortical structures on iEC mapping in greater depth.

Online content

Any methods, additional references, Nature Portfolio reporting summaries, source data, extended data, supplementary information, acknowledgements, peer review information; details of author contributions and competing interests; and statements of data and code availability are available at https://doi.org/10.1038/s41593-026-02389-8.

References

1. Felleman, D. J. & Van Essen, D. C. Distributed hierarchical processing in the primate cerebral cortex. *Cereb. Cortex* **1**, 1–47 (1991).
2. Bastos, A. M. et al. Visual areas exert feedforward and feedback influences through distinct frequency channels. *Neuron* **85**, 390–401 (2015).
3. Huntenburg, J. M., Bazin, P.-L. & Margulies, D. S. Large-scale gradients in human cortical organization. *Trends Cogn. Sci.* **22**, 21–31 (2018).
4. Froudist-Walsh, S. et al. A dopamine gradient controls access to distributed working memory in the large-scale monkey cortex. *Neuron* **109**, 3500–3520 (2021).
5. García-Cabezas, M. Á., Hacker, J. L. & Zikopoulos, B. A protocol for cortical type analysis of the human neocortex applied on histological samples, the atlas of von Economo and Koskinas, and magnetic resonance imaging. *Front. Neuroanat.* **14**, 576015 (2020).
6. Foit, N. A. et al. A whole-brain 3D myeloarchitectonic atlas: mapping the Vogt-Vogt legacy to the cortical surface. *Neuroimage* **263**, 119617 (2022).
7. Markov, N. T. et al. Anatomy of hierarchy: feedforward and feedback pathways in macaque visual cortex. *J. Comp. Neurol.* **522**, 225–259 (2014).
8. Margulies, D. S. et al. Situating the default-mode network along a principal gradient of macroscale cortical organization. *Proc. Natl Acad. Sci. USA* **113**, 12574–12579 (2016).
9. Mesulam, M.-M. *Principles of Behavioral and Cognitive Neurology* (Oxford Univ. Press, 2000).
10. Samara, A., Eilbott, J., Margulies, D. S., Xu, T. & Vanderwal, T. Cortical gradients during naturalistic processing are hierarchical and modality-specific. *Neuroimage* **271**, 120023 (2023).
11. Wang, X., Margulies, D. S., Smallwood, J. & Jefferies, E. A gradient from long-term memory to novel cognition: transitions through default mode and executive cortex. *Neuroimage* **220**, 117074 (2020).
12. Murphy, C. et al. Modes of operation: a topographic neural gradient supporting stimulus dependent and independent cognition. *Neuroimage* **186**, 487–496 (2019).
13. Dong, D. et al. Compressed sensorimotor-to-transmodal hierarchical organization in schizophrenia. *Psychol. Med.* **53**, 771–784 (2023).
14. Hong, S.-J. et al. Atypical functional connectome hierarchy in autism. *Nat. Commun.* **10**, 1022 (2019).
15. Sydnor, V. J. et al. Intrinsic activity development unfolds along a sensorimotor-association cortical axis in youth. *Nat. Neurosci.* **26**, 638–649 (2023).
16. Andrews, B., Ramsey, J., Sanchez-Romero, R., Camchong, J. & Kummerfeld, E. Fast scalable and accurate discovery of DAGs using the best order score search and grow-shrink trees. In *Advances in Neural Information Processing Systems* 36 (NeurIPS 2023).
17. Frässle, S. et al. Regression DCM for fMRI. *Neuroimage* **155**, 406–421 (2017).
18. Reid, A. T. et al. Advancing functional connectivity research from association to causation. *Nat. Neurosci.* **22**, 1751–1760 (2019).
19. Mumford, J. A. & Ramsey, J. D. Bayesian networks for fMRI: a primer. *Neuroimage* **86**, 573–582 (2014).
20. Ramsey, J. D., Sanchez-Romero, R. & Glymour, C. Non-Gaussian methods and high-pass filters in the estimation of effective connections. *Neuroimage* **84**, 986–1006 (2014).
21. Sanchez-Romero, R. et al. Estimating feedforward and feedback effective connections from fMRI time series: assessments of statistical methods. *Netw. Neurosci.* **3**, 274–306 (2019).
22. Crimi, A., Dodero, L., Sambataro, F., Murino, V. & Sona, D. Structurally constrained effective brain connectivity. *Neuroimage* **239**, 1022 (2021).
23. Schwab, S. et al. Directed functional connectivity using dynamic graphical models. *Neuroimage* **175**, 340–353 (2018).
24. Smith, S. M. et al. Network modelling methods for FMRI. *Neuroimage* **54**, 875–891 (2011).
25. David, O. fMRI connectivity, meaning and empiricism: comments on: Roebroeck et al. The identification of interacting networks in the brain using fMRI: model selection, causality and deconvolution. *Neuroimage* **58**, 306–309; author reply 310–311 (2011).
26. Allegra, M., Gilson, M. & Brovelli, A. Directed neural interactions in fMRI: a comparison between Granger causality and effective connectivity. Preprint at *bioRxiv* https://doi.org/10.1101/2024.02.22.581068 (2024).
27. Razi, A. et al. Large-scale DCMs for resting-state fMRI. *Netw. Neurosci.* **1**, 222–241 (2017).
28. Schaefer, A. et al. Local–global parcellation of the human cerebral cortex from intrinsic functional connectivity MRI. *Cereb. Cortex* **28**, 3095–3114 (2018).
29. Glasser, M. F. et al. A multi-modal parcellation of human cerebral cortex. *Nature* **536**, 171–178 (2016).
30. Schlösser, R. G. M. et al. Fronto-cingulate effective connectivity in major depression: a study with fMRI and dynamic causal modeling. *Neuroimage* **43**, 645–655 (2008).
31. Sharaev, M. G., Zavyalova, V. V., Ushakov, V. L., Kartashov, S. I. & Velichkovsky, B. M. Effective connectivity within the default mode network: dynamic causal modeling of resting-state fMRI data. *Front. Hum. Neurosci.* **10**, 14 (2016).
32. Mill, R. D., Bagic, A., Bostan, A., Schneider, W. & Cole, M. W. Empirical validation of directed functional connectivity. *Neuroimage* **146**, 275–287 (2017).
33. Seguin, C., Razi, A. & Zalesky, A. Inferring neural signalling directionality from undirected structural connectomes. *Nat. Commun.* **10**, 4289 (2019).
34. Frässle, S. et al. Whole-brain estimates of directed connectivity for human connectomics. *Neuroimage* **225**, 117491 (2021).
35. Bastos, A. M. et al. Canonical microcircuits for predictive coding. *Neuron* **76**, 695–711 (2012).
36. Shen, S. et al. Distinct organization of two cortico-cortical feedback pathways. *Nat. Commun.* **13**, 6389 (2022).

37. Sancha-Velasco, A., Uceda-Heras, A. & García-Cabezas, M. Á. Cortical type: a conceptual tool for meaningful biological interpretation of high-throughput gene expression data in the human cerebral cortex. *Front. Neuroanat.* **17**, 1187280 (2023).
38. Cooper, S. J. From Claude Bernard to Walter Cannon. Emergence of the concept of homeostasis. *Appetite* **51**, 419–427 (2008).
39. Lütkepohl, H. *New Introduction to Multiple Time Series Analysis* (Springer, 2005).
40. Barnett, L. & Seth, A. K. The MVGC multivariate Granger causality toolbox: a new approach to Granger-causal inference. *J. Neurosci. Methods* **223**, 50–68 (2014).
41. Richardson, T. S. A discovery algorithm for directed cyclic graphs. In *Proc. 12th Conference on Uncertainty in Artificial Intelligence* 454–461 (Morgan Kaufmann, 1996).
42. Hyvärinen, A. & Smith, S. M. Pairwise likelihood ratios for estimation of non-Gaussian structural equation models. *J. Mach. Learn. Res.* **14**, 111–152 (2013).
43. Lam, W.-Y., Andrews, B. & Ramsey, J. Greedy relaxations of the sparsest permutation algorithm. In *Proc. 38th Conference on Uncertainty in Artificial Intelligence* 1052–1062 (PMLR, 2022).
44. Patel, R. S., Bowman, F. D. & Rilling, J. K. A Bayesian approach to determining connectivity of the human brain. *Hum. Brain Mapp.* **27**, 267–276 (2006).
45. Milham, M. P. et al. An open resource for non-human primate imaging. *Neuron* **100**, 61–74 (2018).
46. Wu, G.-R. et al. rsHRF: a toolbox for resting-state HRF estimation and deconvolution. *Neuroimage* **244**, 118591 (2021).
47. Nozari, E. et al. Macroscopic resting-state brain dynamics are best described by linear models. *Nat. Biomed. Eng.* **8**, 68–84 (2024).
48. Vezoli, J. et al. Cortical hierarchy, dual counterstream architecture and the importance of top-down generative networks. *Neuroimage* **225**, 117479 https://doi.org/10.1016/j.neuroimage.2020.117479 (2021).
49. De Pasquale, R. & Sherman, S. M. Synaptic properties of corticocortical connections between the primary and secondary visual cortical areas in the mouse. *J. Neurosci.* **31**, 16494–16506 (2011).
50. Javadzadeh, M. & Hofer, S. B. Dynamic causal communication channels between neocortical areas. *Neuron* **110**, 2470–2483 (2022).
51. Deco, G., Kringelbach, M. L., Jirsa, V. K. & Ritter, P. The dynamics of resting fluctuations in the brain: metastability and its dynamical cortical core. *Sci. Rep.* **7**, 3095 https://doi.org/10.1038/s41598-017-03073-5 (2017).
52. Zhang, S. et al. In vivo whole-cortex marker of excitation-inhibition ratio indexes cortical maturation and cognitive ability in youth. *Proc. Natl Acad. Sci. USA* **121**, e2318641121 (2024).
53. Kong, X. et al. Sensory-motor cortices shape functional connectivity dynamics in the human brain. *Nat. Commun.* **12**, 6373 https://doi.org/10.1038/s41467-021-26704-y (2021).
54. Mitra, A., Snyder, A. Z., Hacker, C. D. & Raichle, M. E. Lag structure in resting-state fMRI. *J. Neurophysiol.* **111**, 2374–2391 (2014).
55. Ercsey-Ravasz, M. et al. A predictive network model of cerebral cortical connectivity based on a distance rule. *Neuron* **80**, 184–197 (2013).
56. Yeo, B. T. T. et al. The organization of the human cerebral cortex estimated by intrinsic functional connectivity. *J. Neurophysiol.* **106**, 1125–1165 (2011).
57. Parkes, L. et al. Asymmetric signaling across the hierarchy of cytoarchitecture within the human connectome. *Sci. Adv.* **8**, eadd2185 (2022).
58. Mesulam, M. M. From sensation to cognition. *Brain* **121**, 1013–1052 (1998).
59. Pijnenburg, R. et al. Myelo- and cytoarchitectonic microstructural and functional human cortical atlases reconstructed in common MRI space. *Neuroimage* **239**, 118274 https://doi.org/10.1016/j.neuroimage.2021.118274 (2021).
60. Burt, J. B. et al. Hierarchy of transcriptomic specialization across human cortex captured by structural neuroimaging topography. *Nat. Neurosci.* **21**, 1251–1259 (2018).
61. Barbas, H. General cortical and special prefrontal connections: principles from structure to function. *Annu. Rev. Neurosci.* **38**, 269–289 (2015).
62. Kringelbach, M. L., Perl, Y. S., Tagliazucchi, E. & Deco, G. Toward naturalistic neuroscience: mechanisms underlying the flattening of brain hierarchy in movie-watching compared to rest and task. *Sci. Adv.* **9**, eade6049 (2023).
63. Khorsand, P., Moore, T. & Soltani, A. Combined contributions of feedforward and feedback inputs to bottom-up attention. *Front. Psychol.* **6**, 155 (2015).
64. Debes, S. R. & Dragoi, V. Suppressing feedback signals to visual cortex abolishes attentional modulation. *Science* **379**, 468–473 (2023).
65. Chen, W. G. et al. The emerging science of interoception: sensing, integrating, interpreting, and regulating signals within the self. *Trends Neurosci.* **44**, 3–16 (2021).
66. Hubel, D. H. & Wiesel, T. N. Receptive fields, binocular interaction and functional architecture in the cat's visual cortex. *J. Physiol.* **160**, 106–154 (1962).
67. Hilgetag, C.-C., O'Neill, M. A. & Young, M. P. Hierarchical organization of macaque and cat cortical sensory systems explored with a novel network processor. *Philos. Trans. R. Soc. Lond. B* **355**, 71–89 (2000).
68. Hilgetag, C. C. & Goulas, A. 'Hierarchy' in the organization of brain networks. *Philos. Trans. R. Soc. Lond. B* **375**, 20190319 (2020).
69. Mayer, J., Schuster, H. G. & Claussen, J. C. Role of inhibitory feedback for information processing in thalamocortical circuits. *Phys. Rev. E* **73**, 031908 (2006).
70. van Kerkoerle, T. et al. Alpha and gamma oscillations characterize feedback and feedforward processing in monkey visual cortex. *Proc. Natl Acad. Sci. USA* **111**, 14332–14341 (2014).
71. Li, W.-C., Soffe, S. R., Wolf, E. & Roberts, A. Persistent responses to brief stimuli: feedback excitation among brainstem neurons. *J. Neurosci.* **26**, 4026–4035 (2006).
72. Yang, W., Carrasquillo, Y., Hooks, B. M., Nerbonne, J. M. & Burkhalter, A. Distinct balance of excitation and inhibition in an interareal feedforward and feedback circuit of mouse visual cortex. *J. Neurosci.* **33**, 17373–17384 (2013).
73. Weiler, S. et al. A primary sensory cortical interareal feedforward inhibitory circuit for tacto-visual integration. *Nat. Commun.* **15**, 3081 (2024).
74. Zeki, S. & Shipp, S. The functional logic of cortical connections. *Nature* **335**, 311–317 (1988).
75. Girard, P., Salin, P. A. & Bullier, J. Visual activity in areas V3a and V3 during reversible inactivation of area V1 in the macaque monkey. *J. Neurophysiol.* **66**, 1493–1503 (1991).
76. Vezoli, J. et al. Quantitative analysis of connectivity in the visual cortex: extracting function from structure. *Neuroscientist* **10**, 476–482 (2004).
77. Garrido, M. I., Kilner, J. M., Kiebel, S. J. & Friston, K. J. Evoked brain responses are generated by feedback loops. *Proc. Natl Acad. Sci. USA* **104**, 20961–20966 (2007).
78. Harrison, L. M., Stephan, K. E., Rees, G. & Friston, K. J. Extra-classical receptive field effects measured in striate cortex with fMRI. *Neuroimage* **34**, 1199–1208 (2007).
79. Shine, J. M., Lewis, L. D., Garrett, D. D. & Hwang, K. The impact of the human thalamus on brain-wide information processing. *Nat. Rev. Neurosci.* **24**, 416–430 (2023).
80. Wang, H. E. et al. Delineating epileptogenic networks using brain imaging data and personalized modeling in drug-resistant epilepsy. *Sci. Transl. Med.* **15**, eabp8982 (2023).

81. Demirtaş, M. et al. Hierarchical heterogeneity across human cortex shapes large-scale neural dynamics. *Neuron* **101**, 1181–1194 (2019).
82. Deco, G. et al. Resting-state functional connectivity emerges from structurally and dynamically shaped slow linear fluctuations. *J. Neurosci.* **33**, 11239–11252 (2013).
83. Mejias, J. F., Murray, J. D., Kennedy, H. & Wang, X.-J. Feedforward and feedback frequency-dependent interactions in a large-scale laminar network of the primate cortex. *Sci. Adv.* **2**, e1601335 (2016).
84. Mejías, J. F. & Wang, X.-J. Mechanisms of distributed working memory in a large-scale network of macaque neocortex. *eLife* **11**, e72136 (2022).
85. Pang, J. C. et al. Geometric constraints on human brain function. *Nature* **618**, 566–574 (2023).
86. Faskowitz, J. et al. Commentary on Pang et al. (2023). *Nature*. Preprint at *bioRxiv* https://doi.org/10.1101/2023.07.20.549785 (2023).
87. Friston, K. J., Harrison, L. & Penny, W. Dynamic causal modelling. *Neuroimage* **19**, 1273–1302 (2003).
88. Liu, Z.-Q. et al. Benchmarking methods for mapping functional connectivity in the brain. *Nat. Methods* **22**, 1593–1602 (2025).
89. Masharipov, R., Knyazeva, I., Korotkov, A., Cherednichenko, D. & Kireev, M. Comparison of whole-brain task-modulated functional connectivity methods for fMRI task connectomics. *Commun. Biol.* **7**, 1402 (2024).

Methods

Data acquisition

Macaque tract-tracing data. For gold-standard directional validation, we leveraged macaque tract-tracing data from a previous study[4]. The tracers injected into specific cortical targets were transported to neuron cell bodies across the brain, except the injection site. These neurons, termed labeled neurons (LNs), were quantified in source areas projecting to the target. Connection strength was defined as FLN: source area LNs divided by total LNs, excluding the injection site. This dataset also provides SLNs, which indicate the proportion of LNs in layers II and III. This ratio characterizes the FF nature of the connections[1,7]: a higher (or lower) SLN indicates that the cortical region predominantly involves FF (or FB) pathways.

Macaque neuroimaging data and preprocessing. We also analyzed 3-T resting-state fMRI data from 19 anesthetized macaques in PRIME-DE database (University of California, Davis site)[45]. Data were acquired using a Siemens Skyra scanner with a four-channel clamshell coil (1.4-mm isotropic voxels; repetition time (TR) = 1,600 ms, echo time (TE) = 24 ms and field of view (FOV) = 140 mm). We preprocessed the MRI data using the HCP minimal preprocessing pipeline[90], encompassing gradient and susceptibility distortion correction, motion correction, cortical surface reconstruction, surface resampling to a standard tessellated mesh and alignment to a grayordinate space. The fMRI time series were denoised using 12 motion-related regressors plus derivatives and five principal components from white matter and ventricles and their derivatives (32 regressors in total), then high-pass filtered at 0.008 Hz.

Human neuroimaging data and preprocessing. Three human fMRI datasets were analyzed: resting, movie watching and tonic-pain states. For resting state, we analyzed the S1200-release data from HCP and retained 440 participants after excluding excessive motion (mean framewise displacement > 0.2 mm; mean age 28.8 years; 245 females). For movie watching, we used the data 'StudyForrest'[91] and retained 13 participants, excluding two participants with excessive head motion (mean framewise displacement > 0.2 mm; mean age 29.4 years; six females). Finally, for tonic-pain state, we reused data from a previous study[92], including 48 participants (mean age 22.8 years; 21 females) after excluding four participants who reported higher avoidance ratings during the control run than during the capsaicin run and one participant with insufficient MRI brain coverage.

HCP data were acquired on a 3-T Siemens Connectome Skyra with a 32-channel receive head coil. T1-weighted structural images were acquired with 0.7-mm isotropic voxels (TR = 2,400 ms, TE = 2.14 ms and FOV = 224 mm × 224 mm). The StudyForrest data were acquired while participants watched the movie, *Forrest Gump*, on 3-T Philips Achieva dStream scanner with a 32-channel head coil. T1-weighted structural images were captured with 0.67-mm isotropic voxels (TR = 2,500 ms, TE = 5.7 ms and FOV = 191.8 mm × 256 mm × 256 mm). In the tonic pain dataset, capsaicin-rich hot sauce was applied to participants' tongues while they continuously rated pain intensity during a 20-min scan. T1-weighted structural images were acquired on a 3-T Siemens Prisma scanner with a 64-channel head coil (0.7-mm isotropic voxels; TR = 2,400 ms, TE = 2.34 ms and FOV = 224 mm × 224 mm).

fMRI preprocessing. Our fMRI preprocessing adhered as closely to the original HCP pipeline[90] as possible across all datasets to maintain consistency. These included correction of spatial and gradient distortions and head motion, intensity normalization, bias-field removal, registration to T1-weighted structural images and transformation to 2-mm Montreal Neurological Institute (MNI) space. Structured noise was removed with ICA-FIX for HCP data[93]. For the movie-watching and tonic pain datasets, we employed ICA-AROMA, which operates on a conceptual basis similar to ICA-FIX but is designed for general (non-HCP) datasets. In addition, we regressed out the mean cerebrospinal fluid and white matter signals and high-pass filtered the data at 0.008 Hz. Parcel-level time series were computed by averaging the time series for every vertex within each region of the Schaefer-100 or MMP-360 atlas.

Diffusion MRI and SC. To construct an SC matrix for a simulation purpose, we employed independent HCP Q3 diffusion-weighted MRI from 86 young adult participants. The detailed information on the magnetic resonance sequences and preprocessing pipelines is thoroughly documented in the original paper[94].

After the preprocessing steps, we first estimated fiber orientation distributions from diffusion-weighted MRI with multishell, multitissue constrained spherical deconvolution in MRtrix3[95]. We then ran a deterministic tractography algorithm to construct the tractogram from the estimated fibers, employing the algorithm's default settings (except for maximum streamline length (250 mm) and number of streamlines (five million)), and performed SIFT2 filtering[96]. Group-level SC matrices were then generated by counting streamlines between the parcels in both Schaefer-100[28] and MMP-360[29] atlases and averaging them across subjects.

EC algorithms

In this study, we included a diverse set of nine EC algorithms (Extended Data Table 1), each previously benchmarked for their ability to estimate directionality and representing the field's major methodological paradigms.

Rather than developing a new algorithm, we unified existing approaches into a cohesive, generalizable framework to leverage their complementary strengths (iEC). A cornerstone of this framework is a new taxonomy that classifies these algorithms into two principal families: (1) dynamical systems and (2) graphical models. This classification is substantiated not only by their distinct theoretical assumptions but also by empirical, data-driven clustering of the EC results from each algorithm (Extended Data Fig. 1).

Dynamical systems category. Dynamical systems methods assume that observed brain signals are generated by interacting components evolving over time. These models formalize interactions through differential equations, often in continuous time. Directional influences are embedded in the system's temporal evolution, allowing directionality to be inferred from how past activity shapes future dynamics. Because they explicitly track how regional activity evolves in response to others, they inherently accommodate recurrent interactions such as FB loops. Moreover, by modeling the magnitude and sign of influence, they represent both excitatory and inhibitory effects between regions.

(1) rDCM[17] is a computationally efficient implementation of DCM that infers directed interactions by fitting a Bayesian linear regression model in the frequency domain. Assuming a fixed canonical HRF, this algorithm simplifies an underlying generative model, yet performs comparably to spectral DCM, particularly for resting-state fMRI data.

(2) VAR[39] is a linear autoregressive model that estimates directional influence by assessing how past activity in one region predicts future activity in another. We applied a first-order VAR model, following previous studies showing limited gain from higher orders given the low temporal resolution of fMRI[47]. To reduce overfitting, we applied L2 regularization to the least-squares estimation of the VAR coefficient matrix. The regularization parameter λ was optimized using a training dataset to maximize predictive accuracy with respect to the ground-truth target (for example, FLN in the macaque data), as shown in Supplementary Fig. 5.

(3) MVGC[40] extends VAR by testing whether adding the past activity of one region improves the prediction of another region's

future activity. Specifically, it compares a full model, which includes both the target region's own past activity and that of the potential source region, with a restricted model that includes only the target region's own history. A significant improvement in prediction by the full model indicates a directed influence from the source to the target region.

Graphical models category. Graphical models estimate directional dependencies among brain regions by analyzing statistical relationships, without assuming temporal order or a generative mechanism. They operate on contemporaneous statistical structures—pairwise or multivariate—to identify the minimal set of direct interactions explaining the observed dependencies. Directionality is inferred using statistical criteria such as conditional independence (for example, absent connections given a third region), non-Gaussianity in marginal distributions and score-based searches (for example, Bayesian information criterion, shortly BIC) over candidate graphs to optimize model fit and parsimony. These principles enable constructing sparse, interpretable directed networks even without temporal resolution.

(1) FASK[21] is a two-step algorithm that first identifies adjacencies using conditional independence testing and then orients edges based on skewness in the joint distribution. It supports FB loops and works efficiently on high-dimensional data.
(2) CCD[41] is a method that identifies directed connections by checking whether dependencies remain after conditioning on subsets of the remaining regions. Loss of dependence suggests indirect or mediated relationships. Unlike classical Bayes-net algorithms, CCD does not assume acyclicity, allowing the recovery of cyclic (recurrent) pathways.
(3) BOSS[16] is a score-based algorithm that searches over variable ordering to identify the most plausible causal graph. For each ordering, it constructs a directed graph by regressing each node on its predecessors and evaluates the result using a penalized likelihood score (for example, BIC). This method balances model fit and sparsity and accommodates both acyclic and cyclic structures.
(4) In directLiNGAM[42], the model assumes linear relations and non-Gaussian noise to uniquely identify a directed acyclic graph. It infers causal order by iteratively identifying exogenous variables and removing their influences from the data.
(5) GRaSP[43] is an algorithm that estimates sparse directed networks by iteratively adding or removing edges while optimizing a scoring function (for example, BIC). GRaSP allows minimal cyclicity and is particularly effective in high-dimensional settings in which sparse connectivity is expected.
(6) Patel's τ[44] is a pairwise asymmetry-based measure that infers directionality by evaluating how often an activity in one region is accompanied by an activity in another, relative to the reverse pattern.

For graphical models with binary outputs, we employed a subsampling ensemble to obtain stable continuous estimates. Following Bühlmann and van de Geer[97], we generated 100 graphs per algorithm using random subsamples of size $N/2$, drawn without replacement from the full fMRI time series of length N. We then averaged the resulting graphs. Therefore, each edge weight reflected selection frequency across subsamples.

All graphical models (except Patel's τ) were implemented using the Tetrad toolbox (https://github.com/cmu-phil/tetrad), which provides standardized implementations of graphical algorithms. To ensure comparability, we used the BIC score with a penalty value of 2 for all Tetrad-based algorithms[16,21,43]. Other algorithm-specific parameters were left at their default values as provided by the Tetrad developers.

iEC framework. Finally, we performed an integration of the results from individual EC algorithms to construct the iEC:

$$\mathrm{iEC} = \frac{1}{N}\sum_{n=1}^{N} \beta_n \, \mathrm{EC}_n$$

The β coefficients were determined by Bayesian optimization to maximize the objective function ρ:

$$\beta^* = \underset{\beta=\{\beta_1,\ldots,\beta_N\}}{\operatorname{argmax}} \rho\,(\mathrm{iEC}, T)$$

where ρ denotes the correlation between iEC and target matrix T. This target matrix differed across validation stages: (1) the FLN matrix for the macaque analysis; (2) synthetic directed SC for the simulation analysis; and (3) empirical human fMRI signal properties for the human analysis.

Evaluation framework and signal-level modeling

Next, we evaluated individual EC algorithms and iEC in three stages. First, macaque ECs estimated from resting-state fMRI were compared with anatomical connectivity derived from gold-standard tract tracing (FLN) to test the recovery of biologically validated directionality. Second, we generated synthetic directed networks by rewiring diffusion MRI-based SC using the 'randmio_dir_connected.m' function in the Brain Connectivity Toolbox[98]. For each realization, 20% of edges were reassigned while retaining connectedness and preserving degree and clustering structure (pre-rewiring and post-rewiring correlations: $r > 0.9$ for clustering coefficient and $r > 0.78$ for degree distribution). These ground-truth directed networks were then used as coupling matrices to generate oscillatory dynamics via the Hopf model, and EC estimates from the simulated signals were compared back to the ground-truth directed networks. Third, EC estimates inferred from the resting-state fMRI of the human brain were used as long-range coupling matrices in the Hopf model and evaluated based on how well the simulated signals reproduced the functional characteristics of empirical fMRI. Specifically, we computed a composite score, defined as 'Pearson correlation between empirical and simulated FC' minus 'KS distance between their FCD distributions' (overall fit = r − KS).

Hopf whole-brain model. In the simulation-based validation steps, whole-brain signals were generated using the Hopf model. Local dynamics were modeled with Landau–Stuart oscillators, coupled through a long-range connectivity matrix:

$$\frac{dx_i}{dt} = \left[a_i - x_i^2 - y_i^2\right]x_i - \omega_i\, y_i + G\sum_j C_{ij}\,(x_i - x_j) + \epsilon\eta_i\,(t)$$

$$\frac{\mathrm{d}y_i}{\mathrm{d}t} = \left[a_i - x_i^2 - y_i^2\right]y_i + \omega_i x_i + G\sum_j C_{ij}\,(y_i - y_j) + \epsilon\eta_i\,(t)$$

Here, x_i and y_i are state variables describing the local oscillator for region i; a_i is a bifurcation parameter set to −0.01 for all regions to place them near the Hopf bifurcation point; ω_i is an intrinsic frequency of each node, empirically estimated from the peak frequency of its time series; G is a global scaling parameter; C_{ij} is a connectivity matrix (either synthetic SC or EC depending on the analysis); and $\eta_i(t)$ represents additive Gaussian noise with amplitude $\epsilon = 0.02$. Simulations were integrated with the Euler–Maruyama method ($\mathrm{d}t = 0.1$). Hyperparameter settings followed a previous study[51], and the simulation duration matched the empirical fMRI signal after discarding an initial burn-in period.

Balanced excitation–inhibition model. To test whether the simulation results by the Hopf model could be replicated using a more biologically

grounded model, we also implemented the balanced excitation–inhibition model[99]. This neural mass model includes local excitatory and inhibitory populations within each brain region, governed by synaptic conductances mediated by *N*-methyl-D-aspartate and γ-aminobutyric acid receptors. A feedback inhibition control mechanism stabilizes local circuit dynamics by maintaining inhibitory firing rates at ~3 Hz. Regional interactions are mediated by long-range connectivity, and simulated BOLD signals are generated using the Balloon–Windkessel hemodynamic model. Fixed parameters followed those in a previous study[99], and free parameters were tuned to match large-scale empirical signal properties.

Cross-validation strategy. To ensure out-of-sample generalizability of our findings, we separated the training and test data at each validation stage. For macaque data ($N = 19$), we used 8-train/11-test split. For the simulation analysis, we generated 100 independent whole-brain simulations and split them into 20:80 training/test datasets. For the human brain, data from 220 HCP participants were used for training, and data from an independent set of 220 participants were used for testing. Bayesian optimization was performed using MATLAB's 'bayesopt.m', which constructs a probabilistic surrogate model (typically a Gaussian process) to balance exploration and exploitation while searching for the optimal values.

HRF deconvolution. To assess the influence of regional hemodynamic variability on EC estimates, we performed a post hoc control analysis using the data-driven HRF deconvolution method used in a previous study[46]. This method detects spontaneous large-amplitude BOLD transients as pseudo-events, estimates region-specific and subject-specific HRFs with a time-shifted general linear model with canonical basis functions and recovers latent neural signals by Wiener deconvolution in the frequency domain. We repeated the EC analysis on the deconvolved signals and compared them with the original BOLD-based results.

Neuroanatomical data

Cortical types. To validate the biological significance of our EC-based hierarchy findings, we used cortical-type information based on the reevaluated von Economo's micrographs[5]. These data capture laminar complexity, including the development of layer IV, relative prominence of superficial versus deep layers, subdivision of layers, sharpness of laminar boundaries and the presence of large pyramidal neurons in superficial layers. The cortical types assigned to each brain area based on this laminar information range from highly laminated koniocortical and eulaminate cortices to dysgranular and agranular regions with progressively reduced laminar differentiation. To assign cortical types to the MMP-360 atlas, we used the Brodmann cortical atlas along with the cortical-type annotations presented in a previous study[5]. We then projected this annotated Brodmann atlas to the MMP-360 atlas. We tested the linear relationship between cortical types and our EC-based hierarchy levels using the 'fitglm.m' function in MATLAB.

Cytoarchitecture and myeloarchitecture. We further correlated the finding of whole-brain hierarchy with cytoarchitectonic information according to a cortical parcellation of the Campbell atlas[59]. This atlas delineates 17 distinct cortical regions using histological differences in laminar structure and is largely consistent with Mesulam's organizational scheme[9]. For the myeloarchitecture, we used the cortical parcellation of the Vogt–Vogt legacy data described in a previous study[6].

Mesulam's cortical zone. The foundational cortical zones (limbic, paralimbic, heteromodal association, unimodal association and primary sensorimotor) were originally established in the macaque brain. Mesulam inferred the human homologs of these zones in the Brodmann atlas by leveraging evidence of cytoarchitectonics, electrophysiological recordings, functional imaging and the behavioral effects of focal lesions[9]. We mapped this Brodmann-based annotation onto the MMP-360 atlas and subdivided its 22 modules into 27 while preserving the original boundaries of the MMP. This was used to visualize and interpret the whole-brain signal flows across different brain states.

EC profiling

Below, we describe three methods that we used to profile the network characteristics of the whole-brain EC, including connectome profiles, signal flows and the functional hierarchy estimation of the cerebral cortex.

Degree and positive/negative EC ratio. For connectome profiling, we measured weighted in-degree and out-degree from EC matrix, with columns as sources and rows as targets:

$$\text{In}-\text{degree}\,(i) = \sum_{j=1}^{N} |\text{EC}_{ij}| \quad \text{Out}-\text{degree}\,(j) = \sum_{i=1}^{N} |\text{EC}_{ij}|$$

We further computed the proportion of each signed EC (positive and negative). For in-degree:

$$\text{Positive ratio}_{\text{In-degree}}\,(i) = \frac{\sum_{j=1}^{N} I(\text{EC}_{ij} > 0)}{N}$$

$$\text{Negative ratio}_{\text{In-degree}}\,(i) = \frac{\sum_{j=1}^{N} I(\text{EC}_{ij} < 0)}{N}$$

where I is an indicator function that yields 1 if the connection meets the given condition. Out-degree ratios were computed in the same way. Similarity between the target matrices (for example, synthetic directed SC) and inferred ECs was quantified with Pearson correlation using MATLAB's 'corr.m', with FDR correction for multiple comparisons.

Signal flow analysis. To model unconstrained signal propagation on the EC matrix[57], we first normalized the EC matrix:

$$\text{EC} = \frac{\text{EC}}{\lambda(\text{EC})_{\max} + c} - I$$

Here λ is the largest eigenvalue of the EC matrix, $c = 1$ to ensure system stability and I denotes the identity matrix. Signal propagation was then simulated with the linear dynamical system $\dot{x} = \text{EC}x(t)$. For visualization, node-level flows were summarized within the MMP-22 modules, or MMP-27 modules when profiling them across Mesulam's hierarchy subdivisions.

Data-driven iEC-based hierarchy estimation. Finally, we estimated cortical hierarchy using a model adapted from the macaque studies[7]. In the original framework, the proportion of supragranular projections (SLN) predicts the hierarchical distance between the source and target areas[1,100]. Motivated by a series of findings implicating the potential relationship between the signed iEC and FF and FB pathways, we substituted the SLN with iEC and fit the general linear model:

$$g(E[EC_{ij}]) = \boldsymbol{\theta}_i - \boldsymbol{\theta}_j$$

where θ_i is the hierarchical level of area i and g is a link function relating the expected EC_{ij} to hierarchical distance. In matrix form:

$$g(E[\mathbf{Y}]) = X\boldsymbol{\theta}$$

where $\mathbf{Y}$ is the vectorized EC matrix, $\boldsymbol{\theta}$ is the vector of hierarchical levels and X is the incidence matrix describing source–target relations constructed from the EC. Following a previous study[100], we set the link function g to the identity function and solved the equation using least squares. Before fitting, we retained the top 15% of absolute EC weights to balance a trade-off between sensitivity and specificity. The overall hierarchy pattern was stable across thresholds (Supplementary Fig. 6).

Assessment of state-dependent hierarchy changes. To examine the state dependence of functional hierarchy, we repeated the hierarchy estimation across different brain conditions using the movie-watching and tonic-pain datasets, which have been preprocessed with the same pipeline applied to resting-state data. We then quantified their differences in positive/negative signal flow across the MMP-27 modules. Differences (for example, positive out-degree difference between the movie-watching and resting states) were standardized as *z* scores, and significant modules were identified using one-tailed ($\alpha = 0.05$) and two-tailed ($\alpha = 0.025$) thresholds.

Reporting summary

Further information on research design is available in the Nature Portfolio Reporting Summary linked to this article.

Data availability

This study analyzed previously released datasets and atlas resources together with one restricted dataset. HCP S1200 resting-state and diffusion MRI data are available via ConnectomeDB (https://db.humanconnectome.org/). StudyForrest movie-watching data are available via StudyForrest (https://www.studyforrest.org/). PRIME-DE macaque MRI data from the University of California, Davis site are available via PRIME-DE/NITRC (https://fcon_1000.projects.nitrc.org/indi/PRIME/ucdavis.html). Macaque tract-tracing FLN/SLN data are available via https://github.com/seanfw/macaque_hierarchy. The cytoarchitectonic data used in this study were based on the Campbell atlas reconstructions[59] and are available via https://github.com/ggsegverse/ggsegCampbell. The myeloarchitectonic data are available via https://github.com/NOEL-MNI/noelMyelin. Cortical-type annotations were derived from a previous study[5] using published atlas information as described in Methods. All processed derivative data necessary to reproduce the analyses and figures reported in this study are available via https://github.com/COMBINE-SKKU/SignalFlow_Hierarchy. The tonic-pain raw imaging data used in this study are not publicly available. De-identified data may be made available from the corresponding authors upon reasonable request, subject to institutional approval and any applicable data use agreements. Source data are provided with this paper.

Code availability

The custom code used for iEC estimation, signal flow analysis, hierarchy estimation, whole-brain simulations and figure generation is publicly available via https://github.com/COMBINE-SKKU/SignalFlow_Hierarchy.

References

90. Glasser, M. F. et al. The minimal preprocessing pipelines for the Human Connectome Project. *Neuroimage* **80**, 105–124 (2013).
91. Hanke, M. et al. A studyforrest extension, simultaneous fMRI and eye gaze recordings during prolonged natural stimulation. *Sci. Data* **3**, 160092 (2016).
92. Lee, J.-J. et al. A neuroimaging biomarker for sustained experimental and clinical pain. *Nat. Med.* **27**, 174–182 (2021).
93. Salimi-Khorshidi, G. et al. Automatic denoising of functional MRI data: combining independent component analysis and hierarchical fusion of classifiers. *Neuroimage* **90**, 449–468 (2014).
94. Setsompop, K. et al. Pushing the limits of in vivo diffusion MRI for the Human Connectome Project. *Neuroimage* **80**, 220–233 (2013).
95. Tournier, J.-D. et al. MRtrix3: a fast, flexible and open software framework for medical image processing and visualisation. *Neuroimage* **202**, 116137 (2019).
96. Smith, R. E., Tournier, J.-D., Calamante, F. & Connelly, A. SIFT2: enabling dense quantitative assessment of brain white matter connectivity using streamlines tractography. *Neuroimage* **119**, 338–351 (2015).
97. Bühlmann, P. & van de Geer, S. *Statistics for High-Dimensional Data: Methods, Theory and Applications* (Springer, 2011)
98. Rubinov, M. & Sporns, O. Complex network measures of brain connectivity: uses and interpretations. *Neuroimage* **52**, 1059–1069 (2010).
99. Deco, G. et al. How local excitation-inhibition ratio impacts the whole brain dynamics. *J. Neurosci.* **34**, 7886–7898 (2014).
100. Barone, P., Batardiere, A., Knoblauch, K. & Kennedy, H. Laminar distribution of neurons in extrastriate areas projecting to visual areas V1 and V4 correlates with the hierarchical rank and indicates the operation of a distance rule. *J. Neurosci.* **20**, 3263–3281 (2000).

Author contributions

Y.O. designed the study, developed the methodology and code, performed the analyses, generated the figures and wrote the paper. Y.A. contributed to fMRI preprocessing and data processing. J.-J.L. provided the tonic-pain dataset and related methodological input. T.I., S.F.-W., C.P., M.M., R.N.S., D.M. and B.B. contributed to conceptual development, interpretation of the results and critical revision of the paper. C.-W.W. and S.-J.H. provided conceptual guidance, supervised the study and revised the paper. All authors discussed the results, commented on the paper and approved the final version.

Funding

This work was supported by the Institute for Basic Science (IBS-R015-D2; S.-J.H. and C.-W.W.); the National Research Foundation of Korea (NRF) grant funded by the Korean Government (MSIT) (NRF-2022R1C1C1007095, RS-2023-00217361, RS-2024-00398768 and RS-2026-25491191; S.-J.H.); the Natural Sciences and Engineering Research Council of Canada (NSERC Discovery-1304413; B.B.); the Canadian Institutes of Health Research (FDN-154298, PJT-174995 and PJT-191853; B.B.); the SickKids Foundation (NI17-039; B.B.); the Azrieli Centre for Autism Research (ACAR-TACC; B.B.); Brain Canada (Future Leaders and McConnell Brain Imaging Centre Platform; B.B.); Healthy Brains, Healthy Lives (B.B.); the Tier-2 Canada Research Chairs program (B.B.); the Montreal Neurological Institute and its Centre of Excellence in Epilepsy (B.B.); the Helmholtz Association's Initiative and Networking Fund through the Helmholtz International BigBrain Analytics and Learning Laboratory (InterLabs-0015; C.P.); the Deutsche Forschungsgemeinschaft (Grant No. 491111487; C.P.); the National Institutes of Health (NIH; RF1MH128696, R01AG047596, P50MH109429, R01MH124045 and R01MH120482; M.M.); the European Research Council (ERC) under the European Union's Horizon 2020 research and innovation programme (866533-CORTIGRAD; D.M.); and the UKRI Future Leaders Fellowships (UKRI2354) and a UKRI Biotechnology and Biological Sciences Research Council grant (BB/X013243/1; S.F.-W.).

Competing interests

The authors declare no competing interests.

Additional information

Extended data is available for this paper at https://doi.org/10.1038/s41593-026-02389-8.

Supplementary information The online version contains supplementary material available at https://doi.org/10.1038/s41593-026-02389-8.

Correspondence and requests for materials should be addressed to Choong-Wan Woo or Seok-Jun Hong.

Peer review information *Nature Neuroscience* thanks the anonymous reviewers for their contribution to the peer review of this work.

https://doi.org/10.1038/s41593-026-02389-8

Extended Data Table 1 | Summary of EC algorithms used in the iEC framework

Method	1st Category	2nd Category	Linearity	Scope
rDCM	Dynamical systems	Dynamic causal models	Linear	Multivariate
VAR	Dynamical systems	Lag-based	Linear	Multivariate
MVGC	Dynamical systems	Lag-based	Linear	Multivariate
CCD	Graphical model	Hybrid	Nonlinear	Multivariate
FASK	Graphical model	Hybrid	Linear	Multivariate
BOSS	Graphical model	Bayes Net	Linear	Multivariate
GRaSP	Graphical model	Bayes Net	Linear	Multivariate
DirectLiNGAM	Graphical model	Hybrid	Linear	Pairwise
Patel's τ	Graphical model	Hybrid	Nonlinear	Pairwise

Each algorithm is categorized by its primary modeling class, methodological subtype, whether it assumes linear or nonlinear interactions, and whether it operates in a multivariate or pairwise manner.

https://doi.org/10.1038/s41593-026-02389-8

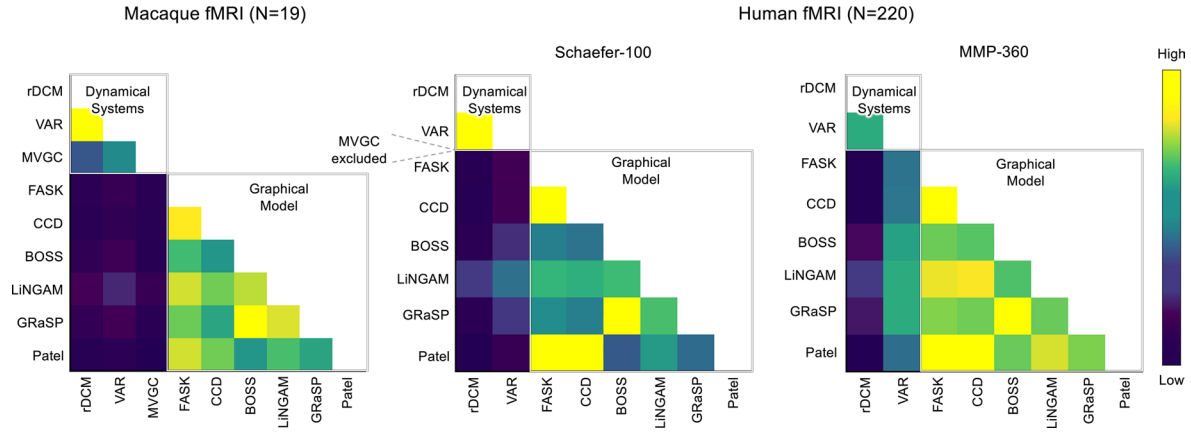

Extended Data Fig. 1 | Similarity of EC patterns across algorithms in macaque and human fMRI datasets. Pairwise Pearson correlations were computed between EC matrices derived from 9 algorithms in the macaque fMRI dataset ($N = 19$ macaque subjects) and 8 algorithms in the human fMRI dataset ($N = 220$ human participants), using both Schaefer-100 and MMP-360 parcellations. The macaque analysis included all 9 algorithms, whereas MVGC was excluded from the human analyses owing to its susceptibility to hemodynamic response function (HRF) variability observed in the macaque dataset. Heat maps indicate Pearson correlation strength between algorithmic outputs (dark blue, low; yellow, high). Across species and parcellations, the analysis revealed consistent clustering of algorithms within theoretical families, notably among Dynamical systems–based methods (for example, rDCM and VAR) and Graphical model–based methods (for example, FASK, CCD and LiNGAM), providing empirical support for the proposed taxonomy of EC algorithms.

https://doi.org/10.1038/s41593-026-02389-8

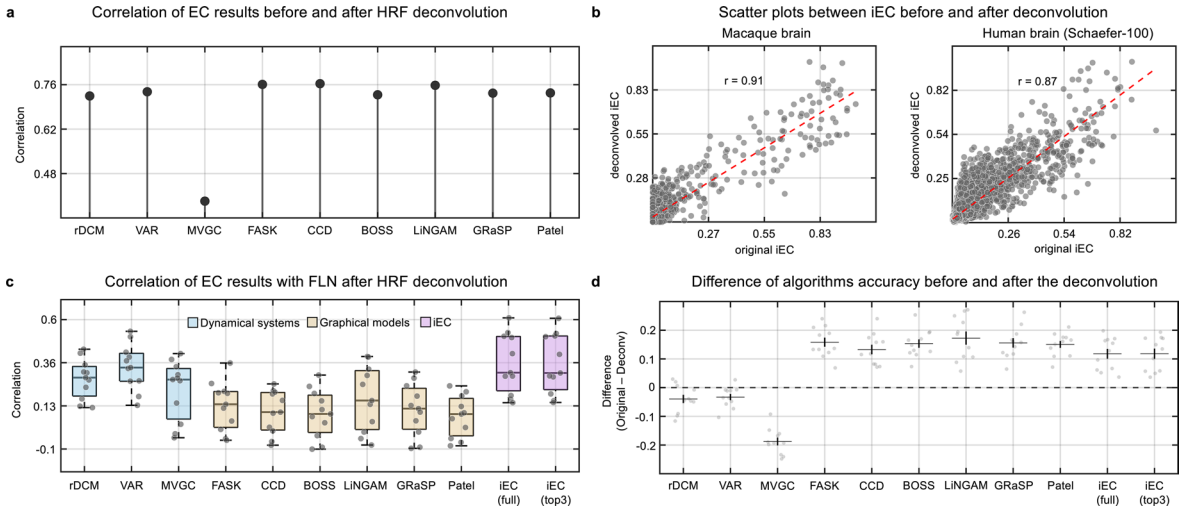

Extended Data Fig. 2 | The impact of HRF deconvolution on the EC estimates. To evaluate the influence of hemodynamic response function (HRF) variability on EC estimation, we applied a blind deconvolution approach, designed to remove region-specific HRFs from observed BOLD signals. **a**, Group-level correlations between EC estimates obtained before and after HRF deconvolution in the macaque brain; each point denotes one algorithm ($n = 9$ algorithms). All algorithms, with the exception of MVGC, exhibited high consistency ($r > 0.8$), suggesting that most methods are robust to HRF variability. **b**, Scatter plots comparing original and deconvolved iEC edge strengths for macaque (left) and human (Schaefer-100 parcellation; right) datasets. Each dot represents a single directed connection. The strong correlations ($r = 0.91$ for macaque; $r = 0.87$ for human) indicate that the iEC framework is stable and resilient to HRF-induced distortions. **c**, Accuracy of EC methods after HRF deconvolution, measured as Pearson correlation with the ground-truth FLN in the independent macaque test set ($n = 11$ macaque subjects, biological replicates; one correlation value per subject). Box plots: center line, median; box limits, 25th and 75th percentiles; whiskers, most extreme points within 1.5× the interquartile range; all data points are overlaid. **d**, Difference in accuracy before versus after HRF deconvolution (original − deconvolved) for the same macaque test subjects. Points denote individual subjects; black horizontal lines and error bars indicate mean ± SEM.

https://doi.org/10.1038/s41593-026-02389-8

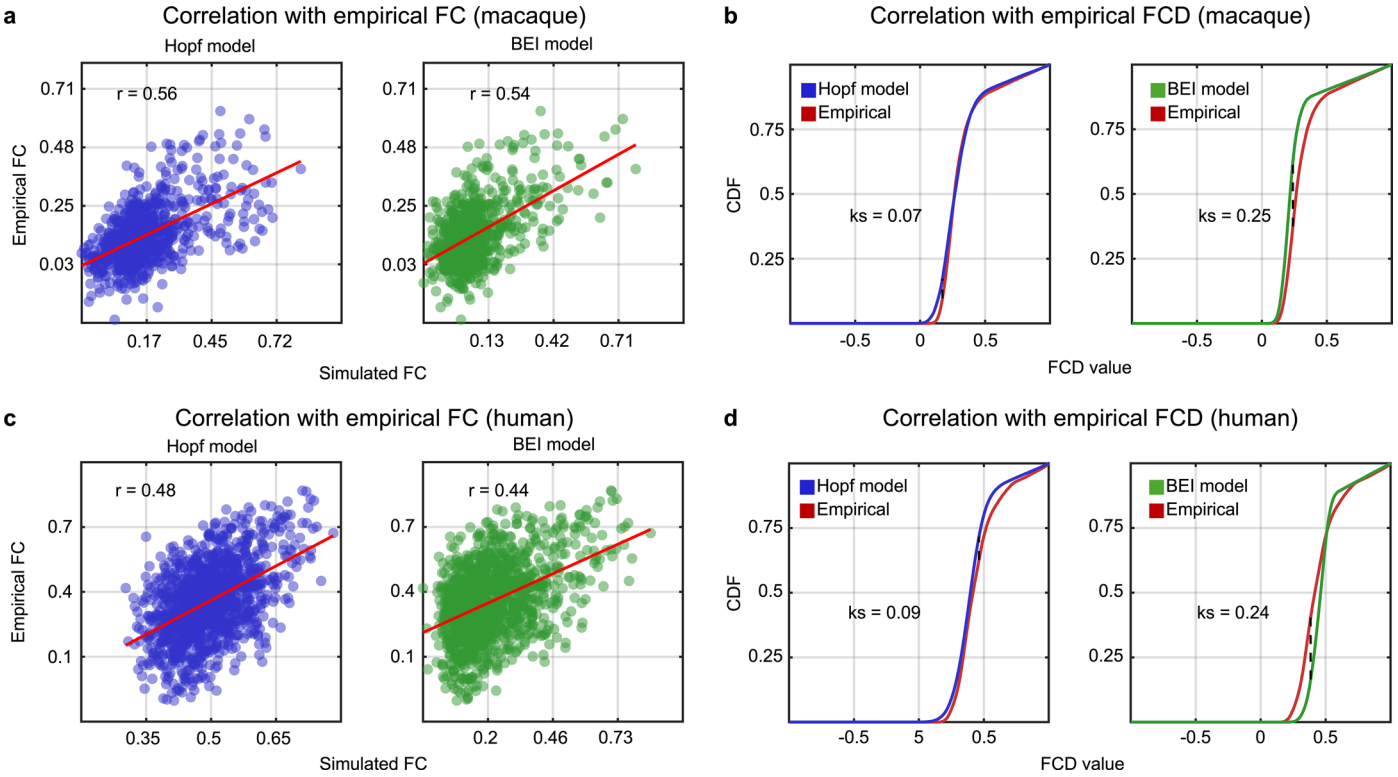

Extended Data Fig. 3 | Comparison of the simulation results between the Hopf model and the biophysical model. The functional connectivity (FC) and functional connectivity dynamics (FCD) obtained from empirical data were compared to those generated by each simulation model. **a**, For macaque data, simulations used the group-level FLN matrix as the directed network backbone. Each dot represents one FC edge, and red lines indicate least-squares linear fits. Both models produced FC patterns that correlated with empirical FC, with the Hopf model showing a slightly higher correlation ($r = 0.56$) than the balanced excitation-inhibition (BEI) model ($r = 0.54$), as indicated by red linear fits. **b**, FCD distributions were evaluated using cumulative distribution functions (CDFs) of the lower-triangular elements of the FCD matrices; similarity to empirical data was assessed using the Kolmogorov–Smirnov (KS) test. The Hopf model more closely matched empirical FCD (KS = 0.07) than the BEI model (KS = 0.25), with the two model distributions differing significantly ($p = 2.0\times10^{27}$, two-sample two-sided KS test comparing model-derived FCD distributions). **c,d**, Same analysis as in (**a,b**), but applied to human fMRI (Schaefer-100). Here, the simulations were based on group-level structural connectivity restricted to the left hemisphere. The Hopf model again showed a higher correlation with empirical FC ($r = 0.48$ vs. 0.44) and a better match to empirical FCD distributions (KS = 0.09 vs. 0.24), with a significant difference between model FCDs ($p = 1.31\times10^{-24}$, two-sample two-sided KS test). These results highlight the Hopf model's sufficient validity to capture both static and dynamic features of empirical brain activities across the two primate species.

https://doi.org/10.1038/s41593-026-02389-8

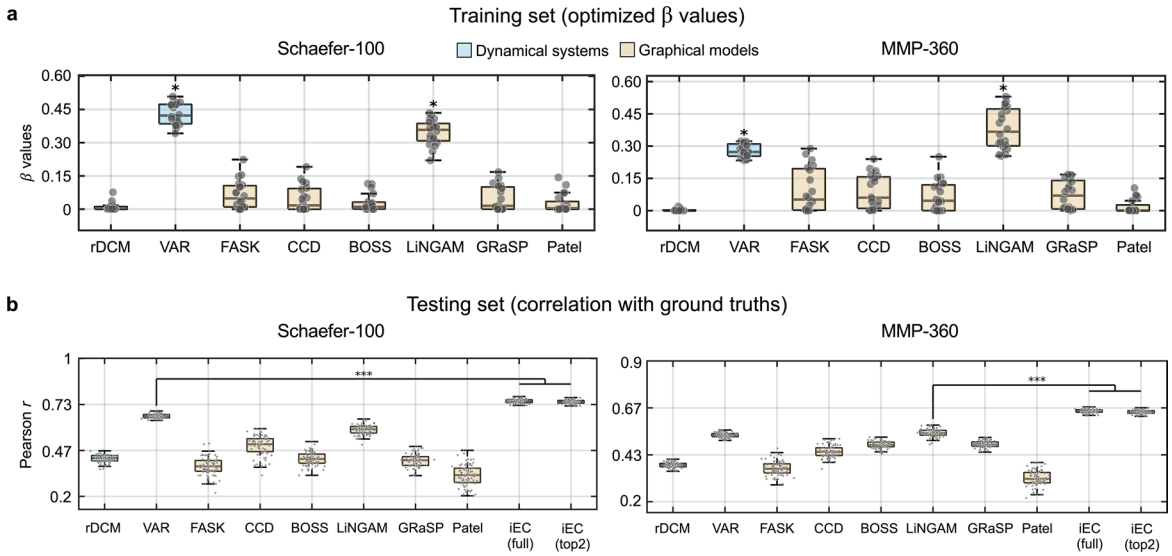

Extended Data Fig. 4 | Simulation-based validation of the iEC framework. **a**, Optimized βs derived from the training data across two parcellations (Schaefer-100 and MMP-360), using $n = 20$ independently generated synthetic directed networks per parcellation in the training set (computational replicates). Each dot denotes one synthetic network. Box plots: center line, median; box limits, 25th and 75th percentiles; whiskers, most extreme points within 1.5× the interquartile range; all data points are overlaid. Asterisks denote significant non-zero β values after one-sided t-tests with FDR correction; Schaefer-100 VAR, $P = 2.94\times10^{-16}$, LiNGAM, $P = 7.74\times10^{-13}$; MMP-360 VAR, $P = 7.40\times10^{-15}$, LiNGAM, $P = 3.92\times10^{-10}$. **b**, Correlation between EC estimates and their directed-SC ground truths in the testing data, with $n = 80$ independently generated synthetic directed networks per parcellation (computational replicates). Each dot denotes one synthetic network. Box plots are defined as in a. The full iEC framework (8 algorithms) outperformed the best-performing individual algorithm at both network resolutions (Schaefer-100 median $r = 0.75$; MMP-360 median $r = 0.65$; two-sided Wilcoxon rank-sum test; $P = 9.39\times10^{-28}$ for both parcellations). The reduced top-3 model (VAR, FASK and LiNGAM) showed similar performance to the full iEC model.

https://doi.org/10.1038/s41593-026-02389-8

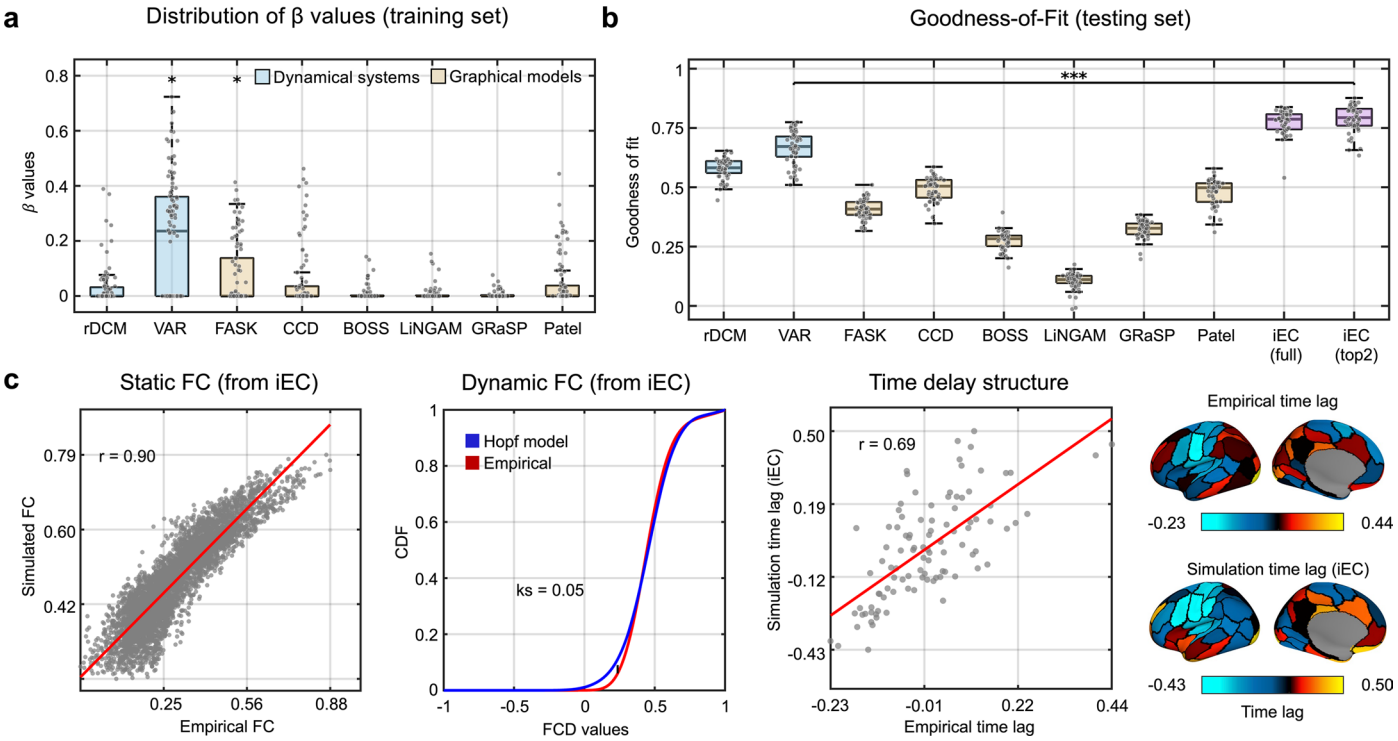

Extended Data Fig. 5 | Validation of iEC framework using human fMRI data (Schaefer-100 atlas). a, Distribution of optimized β values across 50 independent Bayesian optimization runs on the group-average from the training set. Each dot represents one independent optimization run ($n = 50$ computational replicates per algorithm). Box plots: center line, median; box limits, 25th and 75th percentiles; whiskers, most extreme points within 1.5× the interquartile range; all data points are overlaid. Asterisks denote algorithms with significant contributions after two-sided t-tests with FDR correction; VAR, $P = 3.12\times10^{-20}$; FASK, $P = 3.74\times10^{-2}$. **b**, Overall fit scores of EC algorithm and iEC evaluated in a held-out testing set (group-average from $n = 220$ participants; computational replicates). The fit was computed as the static FC correlation minus the FCD KS distance. Box plots are defined as in a. iEC variants (full model and top-2 contributing algorithms) showed higher overall fit than individual EC algorithms. **c**, Comparison of empirical and iEC-simulated FC/FCD. Left, each dot represents one FC edge and the red line indicates the least-squares linear fit. Middle, cumulative distribution functions (CDFs) of FCD from empirical and simulated data; the vertical separation indicates the KS distance. Right, each dot represents the mean time lag of one brain region, and the red line denotes the least-squares linear fit. Group-averaged delay maps are shown on the cortical surface.

https://doi.org/10.1038/s41593-026-02389-8

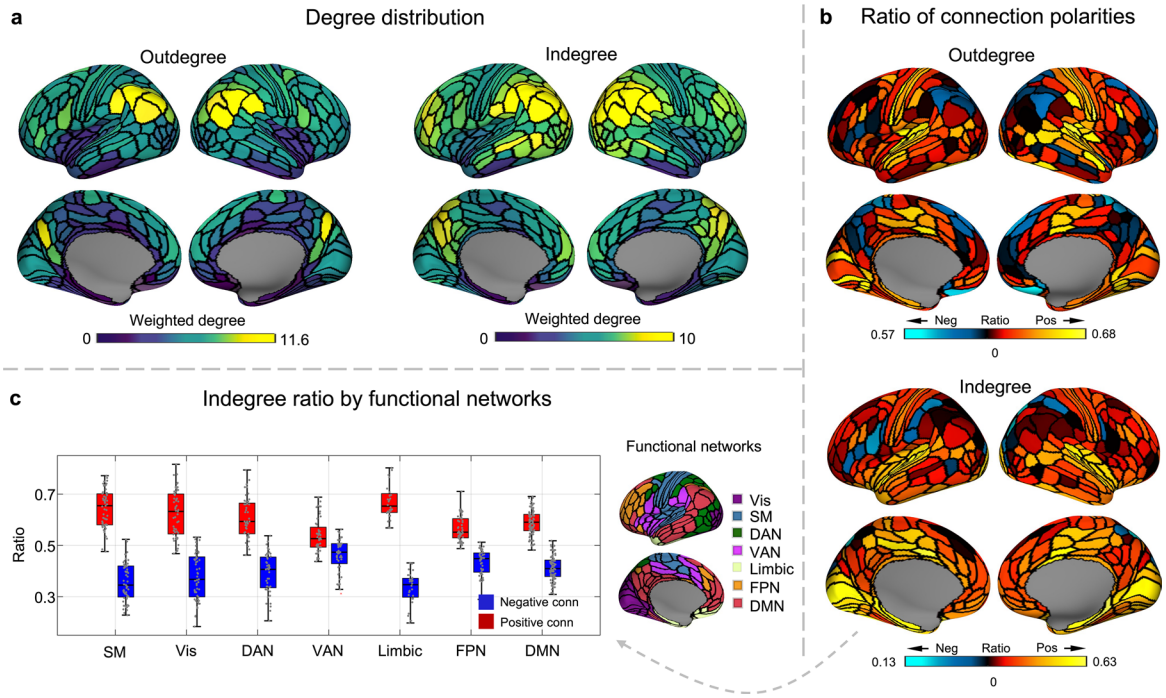

Extended Data Fig. 6 | The iEC network profiling of the resting-state human brain. a, Degree distribution of the iEC. Color bars indicate weighted degree values. **b**, Positive-to-negative ratio of outdegree and indegree connections. Color bars indicate the ratio scale, with cool colors denoting negative-dominant regions and warm colors denoting positive-dominant regions. **c**, Distribution of positive and negative incoming-connection ratios profiled according to the Yeo–Krienen functional networks. Each dot represents one MMP-360 parcel assigned to the indicated functional network (visual, $n = 55$; somatomotor, $n = 55$; dorsal attention, $n = 45$; ventral attention, $n = 48$; limbic, $n = 28$; frontoparietal, $n = 46$; default mode, $n = 83$). Box plots: center line, median; box limits, 25th and 75th percentiles; whiskers, most extreme points within 1.5× the interquartile range; all data points are overlaid. Red indicates positive-connection ratio and blue indicates negative-connection ratio.

https://doi.org/10.1038/s41593-026-02389-8

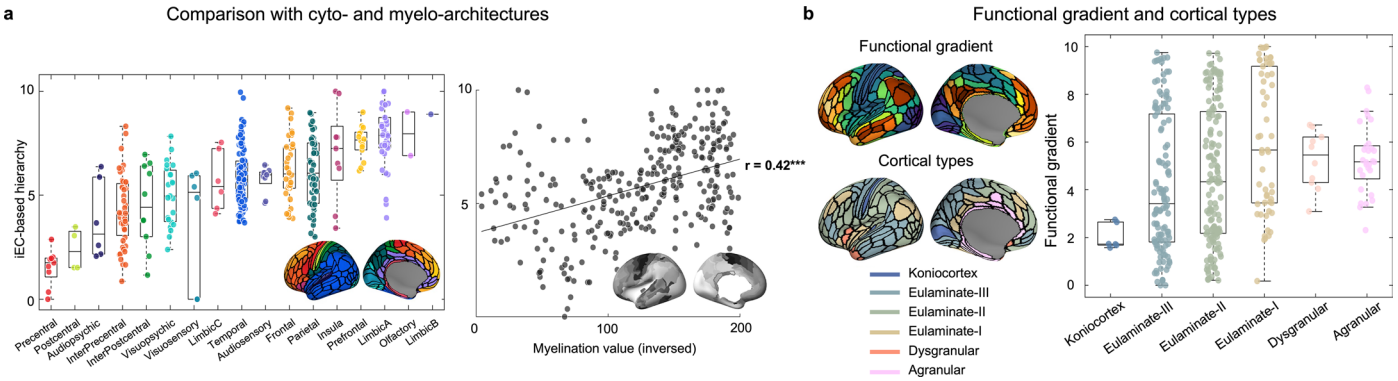

Extended Data Fig. 7 | Functional gradient measured using cortical type atlas. **a**, Left, iEC-based hierarchy values displayed for parcels grouped according to the 17 Campbell cytoarchitectonic regions. Each dot represents one MMP-360 parcel assigned to the indicated Campbell region (Precentral, $n = 9$; Postcentral, $n = 4$; Audiopsychic, $n = 6$; InterPrecentral, $n = 47$; InterPostcentral, $n = 10$; Visuopsychic, $n = 23$; Visuosensory, $n = 6$; LimbicC, $n = 6$; Temporal, $n = 98$; Audiosensory, $n = 9$; Frontal, $n = 36$; Parietal, $n = 46$; Insula, $n = 9$; Prefrontal, $n = 14$; LimbicA, $n = 35$; Olfactory, $n = 2$; LimbicB, $n = 1$). Box plots: center line, median; box limits, 25th and 75th percentiles; whiskers, most extreme points within 1.5× the interquartile range; all data points are overlaid. Right, association between parcel-wise hierarchy values and inverted myelination values; each dot represents one parcel with a valid myeloarchitectural estimate ($n = 319$ valid regions). The solid line indicates the least-squares linear fit (Pearson $r = 0.42$, two-sided $P = 1.18 \times 10^{-14}$. **b**, Functional connectivity gradient values across cortical types. Each dot represents one MMP-360 parcel assigned to the indicated cortical type (koniocortex, $n = 6$; eulaminate-III, $n = 116$; eulaminate-II, $n = 145$; eulaminate-I, $n = 54$; dysgranular, $n = 10$; agranular, $n = 29$). Box plots are defined as in a.

https://doi.org/10.1038/s41593-026-02389-8

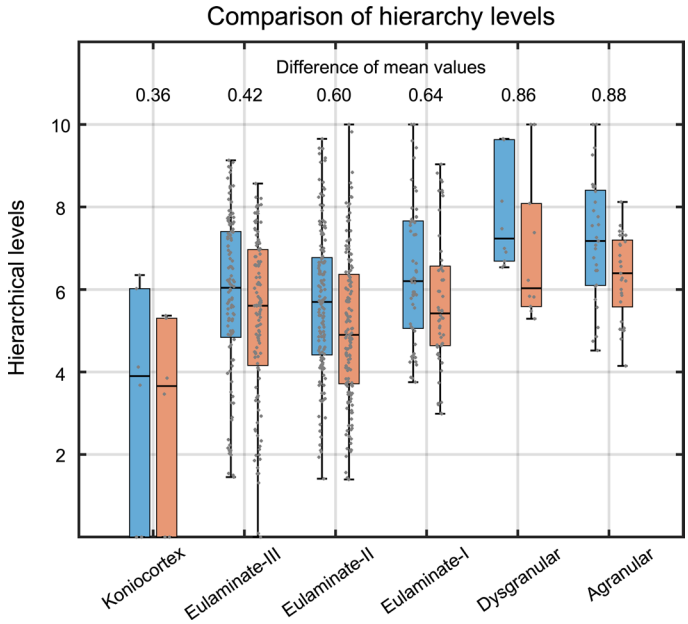

Extended Data Fig. 8 | Impact of negative connections on the signal flow hierarchy. To assess the impact of negative connections on hierarchy estimation, we compared the directed functional hierarchy derived from the original intact iEC (blue) with the hierarchy derived from positive iEC only (orange). Each dot represents one MMP-360 parcel assigned to the indicated cortical type (koniocortex, n = 6; eulaminate-III, n = 116; eulaminate-II, n = 145; eulaminate-I, n = 54; dysgranular, n = 10; agranular, n = 29). Box plots: center line, median; box limits, 25th and 75th percentiles; whiskers, most extreme points within 1.5× the interquartile range; all data points are overlaid. Numbers above each cortical type indicate the difference between mean hierarchical levels of the two models (intact iEC minus positive-only iEC). Differences were smallest in koniocortex and increased toward less-granular cortical types, suggesting that inclusion of negative connections improves hierarchy estimation in higher-order cortical areas.

nature portfolio

Corresponding author(s): Seok-Jun Hong

Last updated by author(s): Apr/27/26

Reporting Summary

Nature Portfolio wishes to improve the reproducibility of the work that we publish. This form provides structure for consistency and transparency in reporting. For further information on Nature Portfolio policies, see our Editorial Policies and the Editorial Policy Checklist.

Statistics

For all statistical analyses, confirm that the following items are present in the figure legend, table legend, main text, or Methods section.

n/a	Confirmed
☐	☒ The exact sample size (*n*) for each experimental group/condition, given as a discrete number and unit of measurement
☐	☒ A statement on whether measurements were taken from distinct samples or whether the same sample was measured repeatedly
☐	☒ The statistical test(s) used AND whether they are one- or two-sided *Only common tests should be described solely by name; describe more complex techniques in the Methods section.*
☐	☒ A description of all covariates tested
☐	☒ A description of any assumptions or corrections, such as tests of normality and adjustment for multiple comparisons
☐	☒ A full description of the statistical parameters including central tendency (e.g. means) or other basic estimates (e.g. regression coefficient) AND variation (e.g. standard deviation) or associated estimates of uncertainty (e.g. confidence intervals)
☐	☒ For null hypothesis testing, the test statistic (e.g. *F*, *t*, *r*) with confidence intervals, effect sizes, degrees of freedom and *P* value noted *Give P values as exact values whenever suitable.*
☒	☐ For Bayesian analysis, information on the choice of priors and Markov chain Monte Carlo settings
☐	☒ For hierarchical and complex designs, identification of the appropriate level for tests and full reporting of outcomes
☐	☒ Estimates of effect sizes (e.g. Cohen's *d*, Pearson's *r*), indicating how they were calculated

Our web collection on statistics for biologists contains articles on many of the points above.

Software and code

Policy information about availability of computer code

Data collection	This study is a secondary analysis of previously acquired datasets; no new data-collection software was used by the authors for the present study. Information on all datasets analyzed in this work is provided in the Data section below. Software, toolboxes, and algorithms used for preprocessing and analysis are listed under Data analysis.
Data analysis	Data analysis was performed primarily in MATLAB R2024b (MathWorks); the public codebase is compatible with MATLAB R2020a or later and was tested on R2023a and R2024a. Java/OpenJDK 11 and cifti-matlab toolbox v2.1.0 were used for Tetrad-based causal-discovery analyses and HCP/CIFTI handling, respectively. Whole-brain effective-connectivity analyses evaluated regression Dynamic Causal Modeling (rDCM v1.2), Vector Autoregression (custom MATLAB implementation; lag order 1), Multivariate Granger Causality (MVGC toolbox; v2), Fast Adjacency Skewness (FASK; Tetrad/causal-cmd v1.12.0), Causal Cyclic Discovery (CCD; Tetrad/causal-cmd v1.12.0), Best Order Score Search (BOSS; Tetrad/causal-cmd v1.12.0), directLiNGAM (Tetrad/causal-cmd v1.12.0), Greedy Relaxation of the Sparsest Permutation (GRaSP; Tetrad/causal-cmd v1.12.0), and Patel's τ (custom MATLAB implementation). Bayesian optimization used MATLAB bayesopt; hierarchy estimation used MATLAB fitglm; graph rewiring used randmio_dir_connected from the Brain Connectivity Toolbox (2019-03-03 release). For HCP resting-state fMRI, we analyzed the ICA-FIX-cleaned CIFTI files distributed as part of the HCP S1200 release. For the StudyForrest and tonic-pain datasets, denoising used ICA-AROMA (v0.4.4). Diffusion MRI processing used MRtrix3 (v3.0.8) for multi-shell multi-tissue constrained spherical deconvolution and tractography. HRF deconvolution used the rsHRF toolbox v2.4.0.

For manuscripts utilizing custom algorithms or software that are central to the research but not yet described in published literature, software must be made available to editors and reviewers. We strongly encourage code deposition in a community repository (e.g. GitHub). See the Nature Portfolio guidelines for submitting code & software for further information.

Data

Policy information about availability of data

All manuscripts must include a data availability statement. This statement should provide the following information, where applicable:

- Accession codes, unique identifiers, or web links for publicly available datasets
- A description of any restrictions on data availability
- For clinical datasets or third party data, please ensure that the statement adheres to our policy

This study analyzed previously released datasets and atlas resources together with one restricted dataset. HCP S1200 resting-state and diffusion MRI data are available through ConnectomeDB (https://db.humanconnectome.org/). StudyForrest movie-watching data are available through StudyForrest (https://www.studyforrest.org/). PRIME-DE macaque MRI data from the UC Davis site are available through PRIME-DE/NITRC (https://fcon_1000.projects.nitrc.org/indi/PRIME/ucdavis.html). Macaque tract-tracing FLN/SLN data are available at https://github.com/seanfw/macaque_hierarchy. Cytoarchitectonic data used in this study were based on the Campbell-atlas reconstructions of Pijnenburg et al. (2021) and can be accessed at https://github.com/ggsegverse/ggsegCampbell. Myeloarchitectonic data are available at https://github.com/NOEL-MNI/noelMyelin. Cortical-type annotations were derived from García-Cabezas et al. (2020). The tonic-pain raw imaging dataset used in this study is not publicly available. Preprocessed derivative data necessary to reproduce the analyses and figures reported here are available at https://github.com/COMBINE-SKKU/SignalFlow_Hierarchy

Research involving human participants, their data, or biological material

Policy information about studies with human participants or human data. See also policy information about sex, gender (identity/presentation), and sexual orientation and race, ethnicity and racism.

Reporting on sex and gender	This study reports self-reported participant sex as a biological attribute. For the HCP dataset, 195 males and 245 females were included; for the StudyForrest dataset, 7 males and 6 females; and for the Tonic-pain dataset, 27 males and 21 females. Sex was not a main target of our hypotheses in this work, thus not included as a variable in the analyses
Reporting on race, ethnicity, or other socially relevant groupings	HCP data were not originally grouped by race, ethnicity, or other socially relevant groupings.
Population characteristics	For the HCP dataset, we analyzed data from 440 participants (mean age 28.8 years, 245 females). In the StudyForrest dataset, 13 participants were included (mean age 29.4 years, 6 females). For the Tonic-Pain dataset, data from 48 participants were analyzed (mean age 22.8 years, 21 females).
Recruitment	Subjects were not recruited for the present study
Ethics oversight	The HCP data were acquired following protocols approved by the Washington University Institutional Review Board. For the StudyForrest data, participants provided informed consent for the public sharing of all obtained data in anonymized form, with the study approved by the Ethics Committee of Otto-von-Guericke University. The Tonic-Pain data collection was approved by the Institutional Review Board of Sungkyunkwan University

Note that full information on the approval of the study protocol must also be provided in the manuscript.

Field-specific reporting

Please select the one below that is the best fit for your research. If you are not sure, read the appropriate sections before making your selection.

☒ Life sciences ☐ Behavioural & social sciences ☐ Ecological, evolutionary & environmental sciences

For a reference copy of the document with all sections, see nature.com/documents/nr-reporting-summary-flat.pdf

Life sciences study design

All studies must disclose on these points even when the disclosure is negative.

Sample size	We included all available data from the relevant datasets, after applying several exclusion criteria explained below.
Data exclusions	In our study, we excluded participants exhibiting excessive head motion, defined as a mean framewise displacement greater than 0.2 mm. The HCP S1200 release dataset initially included 1,200 young adults, but after excluding individuals with excessive head motion, the final sample consisted of 440 participants. The StudyForrest dataset initially included 15 participants, but two were excluded, resulting in a final sample of 13. For the Tonic-Pain dataset, 48 healthy participants were included after excluding 4 participants who reported higher avoidance ratings during the control run than during the capsaicin run, and 1 participant whose MRI brain coverage was insufficient.
Replication	Replication of the main results was conducted at the group level using a training dataset (n=220) and a testing dataset (n=220). Additionally, analyses were performed at the resolution of 360 cortical parcels (MMP-360) and replicated at a resolution of 100 cortical parcels (Schaefer-100).
Randomization	No experimental groups exist.

Blinding	No experimental groups exist and therefore blinding is not relevant to the study.

Reporting for specific materials, systems and methods

We require information from authors about some types of materials, experimental systems and methods used in many studies. Here, indicate whether each material, system or method listed is relevant to your study. If you are not sure if a list item applies to your research, read the appropriate section before selecting a response.

Materials & experimental systems

n/a	Involved in the study
☒	☐ Antibodies
☒	☐ Eukaryotic cell lines
☒	☐ Palaeontology and archaeology
☒	☐ Animals and other organisms
☒	☐ Clinical data
☒	☐ Dual use research of concern
☒	☐ Plants

Methods

n/a	Involved in the study
☒	☐ ChIP-seq
☒	☐ Flow cytometry
☐	☒ MRI-based neuroimaging

Plants

Seed stocks	n/a
Novel plant genotypes	n/a
Authentication	n/a

Magnetic resonance imaging

Experimental design

Design type	Resting state / movie watching / tonic-pain functional MRI
Design specifications	Resting state and movie watching MRI experiments do not involve a specific experiment design. To induce tonic pain, we delivered the capsaicin-rich hot sauce onto the participants' tongues, and participants continuously rated their pain during the run. The fMRI scan duration was 20 minutes to fully cover the entire period of sustained pain from its initiation to the complete remission.
Behavioral performance measures	na

Acquisition

Imaging type(s)	Resting-state / movie watching / tonic-pain functional MRI
Field strength	3 Tesla
Sequence & imaging parameters	HCP S1200 dataset: MRI scans were conducted using a customized 3-T Siemens Connectom Skyra scanner equipped with a standard Siemens 32-channel RF receive head coil. T1-weighted structural images were acquired with 0.7-mm isotropic voxels, a TR of 2400 ms, a TE of 2.14 ms, and a field of view (FOV) of 224×224 mm. T2-weighted functional images were obtained with 2.0-mm isotropic voxels, a TR of 720 ms, a TE of 33.1 ms, and an FOV of 208×180 mm. StudyForrest dataset: In this dataset, participants engaged in a naturalistic audio-visual task by watching and listening to the movie Forrest Gump. MRI data were acquired using a 3-T Philips Achieva dStream scanner with a 32-channel head coil. T1-weighted images were captured with 0.67-mm isotropic voxels, a TR of 2500 ms, a TE of 5.7 ms, and an FOV of 191.8×256×256 mm. T2-weighted functional images were acquired with 1.4×1.4×1.5 mm isotropic voxels, a TR of 2000 ms, a TE of 30 ms, and an FOV of 240 mm. Tonic-pain dataset: To induce tonic pain, capsaicin-rich hot sauce was applied to the participants' tongues, and they continuously rated their pain during the run. The fMRI scan duration was 20 minutes, covering the entire period from pain initiation to complete remission. MRI data were acquired using a 3-T Siemens Prisma scanner with a 64-channel

head coil at Sungkyunkwan University. T1-weighted structural images were obtained with 0.7-mm isotropic voxels, a TR of 2400 ms, a TE of 2.34 ms, and an FOV of 224×224 mm. T2-weighted functional images were acquired with 2.7×2.7×2.7 mm isotropic voxels, a TR of 460 ms, a TE of 27.2 ms, and an FOV of 220 mm.

Area of acquisition: Whole brain

Diffusion MRI ☒ Used ☐ Not used

Parameters: To estimate fiber orientation distributions from the preprocessed DWI data, we employed a multi-shell, multi-tissue constrained spherical deconvolution process using MRtrix3. Following this, we used a deterministic tractography algorithm to construct the tractogram from the estimated fibers. The algorithm's default settings were applied, with modifications to the maximum streamline length (250 mm) and the number of streamlines (5 million).

Preprocessing

Preprocessing software: The preprocessing steps of fMRI data are thoroughly documented in the respective original manuscript for each dataset. In brief, we aimed to adhere as closely as possible to the HCP pipeline across all datasets to maintain consistency. This pipeline includes several critical steps: correcting for spatial and gradient distortions, compensating for head motion, normalizing signal intensity, removing bias fields, aligning data with T1-weighted structural images, and conforming to the 2-mm standard Montreal Neurological Institute space.

Normalization: This pipeline includes several critical steps: correcting for spatial and gradient distortions, compensating for head motion, normalizing signal intensity, removing bias fields, aligning data with T1-weighted structural images, and conforming to the 2-mm standard Montreal Neurological Institute space.

Normalization template: 2-mm standard Montreal Neurological Institute space.

Noise and artifact removal: head motion artifacts and structured noise were mitigated using a combination of independent component analysis and FMRIB's ICA-based X-noiseifier (ICA+FIX). However, it is important to note that this specific classifier is not universally applicable to other neuroimaging data obtained with varying MRI specifications and acquisition protocols. Therefore, for the movie-watching and tonic pain datasets, we opted to employ ICA-AROMA

Volume censoring: The first five volumes were discarded to ensure the fMRI signal reached a steady-state magnetization.

Statistical modeling & inference

Model type and settings: nine distinct effective connectivity algorithms were used the details of which are written in the main script

Effect(s) tested: No effects were tested

Specify type of analysis: ☒ Whole brain ☐ ROI-based ☐ Both

Statistic type for inference: parcel-wise

(See Eklund et al. 2016)

Correction: n/a

Models & analysis

n/a	Involved in the study
☐	☒ Functional and/or effective connectivity
☐	☒ Graph analysis
☐	☒ Multivariate modeling or predictive analysis

Functional and/or effective connectivity: Effective connectivity estimation: we estimated effective connectivity for the entire cortex using nine distinct algorithms. The full list of algorithms is provided in the main manuscript

Graph analysis: The weighted degree was calculated as the sum of the connection weights either from a node (outdegree) or to a node (indegree). To calculate the ratio, we counted the number of positive or negative connections relative to the total number of connections either originating from a node (for outdegree ratio) or terminating at a node (for indegree ratio). Signal flow analysis was conducted by applying the connectivity matrix to a linear dynamical system and solving the system's equations at each subsequent time point (Parkes et al., 2022; Science Advances).

Multivariate modeling and predictive analysis: The hierarchy estimation was performed by fitting a general linear model to the effective connectivity weights, utilizing an incidence matrix that represents the connections between brain regions. The model estimated the beta coefficients, which correspond to the hierarchical values assigned to each brain region.